

Responses to reviewer 1

Manuscript No.: SE-2019-8

Dear reviewer,

I appreciate you for taking the interest and time to make this very thorough and constructive review on the present manuscript. I carefully studied your comments and made necessary changes and corrections to the manuscript. I hope our changes and corrections are sufficient to make our article suitable for publication soon. Your comments and suggestions certainly helped to improve quality and clarity of the paper.

I reply your comments below and highlight the changes (in red color) in the main text according to your suggestions.

Sincerely yours

Tuna Eken

Reviewer 1: The manuscript titled "Moment magnitude estimates for Central Anatolian earthquakes using coda waves" by Tuna Eken addresses the earthquake source characteristics revealed by decomposing the path and source effects in seismic data. Unfortunately, the manuscript is not well prepared: Description of the method is insufficient; some of figures are not correctly cited or never cited; a long review of geology is, however, not related to the discussion; and the discussion lacks some of important studies. It is hard to judge the value of this study from the present form of the manuscript. Detailed comments are listed below:

T.E.: I appreciate reviewer 1 for careful reading. I find the general points that reviewer 1 complains here fairly meaningful. Here in the modified text I considered all critical issues raised by reviewer 1 in details. In that respect I am thankful him since he pointed out deficit of the manuscript in a constructive manner as he suggested solutions to improve current shape of manuscript.

Specific Comments

Reviewer 1: Section 2 (Reginal Setting and Data) has a long description on the geological setting for four paragraphs, however, these are not related to any of discussions. It is nice to review the geological setting, but this can be significantly shortened for improving the readability.

T.E.: I perfectly understand the concern of reviewer 1 and I accordingly shortened Geological part by avoiding some details. The current version of the *Regional Setting* is now made much brief by mainly focusing around tectonic structures responsible observed seismicity that form main database of this study.

Reviewer 1: Section 3 (Method) lacks an explanation on the g parameter. If possible, describe the formula of G as a function of g explicitly, so that it becomes understandable why the Author later used the grid-search scheme for optimizing the g parameter.

T.E.: I appreciate this comment and agree that I missed analytical expression of Green's function. Now I took care of this and added mathematical expression (Now Equation 2 in the revised text) into the text.

Reviewer 1: Figure 4 is cited in L239, however, Figure 4 and the text in L239-244 are inconsistent. Presumably Figure 5 should be cited here. Then Figure 4 is not cited anywhere. Figure 4 looks related to the estimation of the b parameter. Please clarify this.

T.E.: Yes we appreciate reviewer 1. I made a mistake when citing Figure 5. We corrected this. Figure 4 is now also cited properly in the revised version of the text.

Reviewer 1: The paragraph in L258-279 describes the demerit of the assumption of the frequency-independent attenuation factor and the omega-square source model, however, this paragraph should cite other studies already considering these problems. For example, Ide and Beroza (2001, doi: 10.1029/2001GL013106) pointed out the advantage of the empirical Green's function approach and corrected other studies' results one by one. As for the source spectra, Denolle and Shearer (2016, doi: 10.1002/2016JB013105) and Uchide and Imanishi (2016, doi: 10.1785/0120150322) pointed out the deviation of observed source spectra from the conventional omega-square model. Update the discussion by citing these papers.

T.E.: I appreciate this helpful comment and modified relevant part of the manuscript by discussing early works from other parts of the world that have reported deviations from the omega-square model with remarkable similarities to current findings from central Anatolia in this study. Added studies in the *Discussion* section is also updated in *Reference* section.

Reviewer 1: The comparison between the coda-derived moment magnitudes and the local magnitudes was done simply done by the linear regression (equation (9)), however, it has been pointed out that moment magnitudes and local magnitudes are systematically different. Some of papers on this are Bakun and Lindh (1977, BSSA), Edwards et al (2009, doi: 10.1785/0120080292), Goertz-Allmann et al. (2011, doi:10.1785/0120100291), Munafo et al. (2016, doi: 10.1785/0120160130), Malagnini and Munafo (2018, doi: 10.1785/0120170303), and Uchide and Imanishi (2018, doi: 10.1002/2017JB014697). They proposed various types of regression curves, for ex-

ample, composed of two straight line or a polynomial. Update the discussion by citing these papers and correct the abstract (L17-19) accordingly.

T.E.: I appreciate reviewer 1 for making me aware of some early studies in which non-linear form of regression strategy was utilized. I have added the details from those works into Discussion section regarding the comparison between MW-coda and M_L catalogue magnitudes. There I also added a paragraph why we should not expect a perfect match between these two magnitude scales.

Moment magnitude estimates for Central Anatolian earthquakes using coda waves

Tuna Eken¹

¹*Department of Geophysical Engineering, the Faculty of Mines, Istanbul Technical University, 34469 Maslak, Sarıyer, Istanbul, Turkey*

Abstract

Proper estimate of moment magnitude that is a physical measure of the energy released at earthquake source is essential for better seismic hazard assessments in tectonically active regions. Here a coda wave modeling approach that enables the source displacement spectrum modeling of examined event was used to estimate moment magnitude of central Anatolia earthquakes. To achieve this aim, three component waveforms of local earthquakes with magnitudes $2.0 \leq M_L \leq 5.2$ recorded at 72 seismic stations which have been operated between 2013 and 2015 within the framework of the CD-CAT passive seismic experiment. An inversion on the coda wave traces of each selected single event in our database was performed in five different frequency bands between 0.75 and 12 Hz. Our resultant moment magnitudes (M_W -coda) exhibit a good agreement with routinely reported local magnitude (M_L) estimates for study area. Apparent move-out that is, particularly, significant around the scattered variation of M_L - M_W -coda data points for small earthquakes ($M_L < 3.5$) can be explained by possible biases of wrong assumptions to account for anelastic attenuation and of seismic recordings with finite sampling interval. Finally, we present an empirical relation between M_W -coda and M_L for central Anatolian earthquakes.

Keyword(s): Coda waves modelling, seismic moment, moment magnitude, Radiative Transfer Theory

1. Introduction

The robust and stable knowledge of source properties (e.g. moment magnitude estimates) is crucial in seismically active countries such as Turkey for a better evaluation of seismic hazard potential as this highly depends on establishment of reliable seismicity catalogs. Moreover, accurate information on source parameters could be important when developing regional attenuation properties.

Conventional type of magnitude scales (M_L , m_b , M_S) as the result of empirically derived using direct wave analyses can be biased due to various effects such as source radiation pattern, directivity, and heterogeneities along the path since they may cause drastic changes in direct wave amplitude measurements (e.g., Favreau and Archuleta, 2003). Instead several early studies depending on the analysis of local and/or regional coda envelopes have indicated that coda wave amplitudes are significantly less variable by a factor of 3-to-5 compared to direct wave amplitudes (e.g., Mayeda and Walter, 1996; Mayeda et al., 2003; Eken et al., 2004; Malagnini et al., 2004; Gök et al., 2016). In fact local or regional coda waves that are usually considered to be generally to be composed of scattered waves and can be simply explained by that sample the single scattering model of Aki (1969) have been proven to be virtually insensitive to any source radiation pattern effect in contrast to direct waves because of the volume averaging property of the coda waves sampling the entire focal sphere (e.g., Aki and Chouet, 1975; Rautian and Khalturin, 1978). In Sato and Fehler (1998) and Sato et al. (2012)

an extensive review study on the theoretical background of coda generation and advances of empirical observations and modelling efforts can be found in details.

There have been several approaches used for extracting information on earthquake source size via coda wave analyses. These approaches can be mainly divided into two groups. The first group of studies employs coda normalization strategy in which measurements require a correction for seismic attenuation parameters (e.g. intrinsic and scattering) that can be described by some empirical quality factors. To calibrate final source properties reference events are used to adjust measurements with respect to each other. For forward generation of synthetic coda envelopes, either single-backscattering or more advanced multiple-backscattering approximation are used. An example to this group is an empirical method originally developed by Mayeda et al. (2003) to investigate seismic source parameters such as energy, moment, and apparent stress drop in the western United States and in Middle East. They corrected observed coda envelopes for various influences, for instance, path effect, S-to-coda transfer function, site effect, and any distance-dependent changes in coda envelope shape. Empirical coda envelope method have been successfully applied to different regions with complicated tectonics such as northern Italy (e.g. Morasca et al., 2008), Turkey and Middle East (e.g. Eken et al., 2004; Gök et al. 2016); or Korean Peninsula (e.g. Yoo et al., 2013).

Second type of approach is a joint inversion technique that is based on a simultaneous optimization of source, path, and site specific terms via synthetic and observed coda envelope fitting within a selected time window including observed coda and direct-S wave parts. In this approach, the Radiative Transfer Theory (RTT) is employed for analytic expression of synthetic coda wave envelopes. The method that does not rely on coda normalization strategy

was originally developed by Sens-Schönfelder and Wegler (2006) and successfully tested on local and regional earthquakes ($4 \leq M_l \leq 6$) detected by the German Regional Seismic Network. Further it has been applied to investigate source and frequency dependent attenuation properties of different geological settings, i.e., Upper Rhine Graben and Molasse Basin regions in Germany and western Bohemia/Vogtland in Czechia (Eulenfeld and Wegler, 2016); entire United States (2017); central and western North Anatolian Fault Zone (Gäebler et al., 2018; Izgi et al., 2018). A more realistic earth model in which anisotropic scattering conditions were earlier considered by Gusev and Abubakirov (1987) yielded peak broadening effects of the direct seismic wave arrivals. This approach later was used in previous studies (e.g. Zeng, 1993; Przybilla and Korn, 2008; Gäebler et al., 2015) that dealt with propagation of P-wave elastic energy and the effect of conversion between P- and S-wave energies.

In the current work I present estimated source spectra as an output of a joint inversion of S- and coda waves parts of local earthquake waveforms 487 local earthquakes with magnitudes $2.0 < M_L < 4.5$ detected in central Anatolia for their source parameters. The approach used here employs isotropic acoustic RTT approach for forward calculation of synthetic coda envelopes. Gäebler et al. (2015) has observed that modeling results from isotropic scattering were almost comparable with those inferred from relatively more complex elastic RTT simulations with anisotropic scattering conditions. The use of a joint inversion technique is advantageous since it is insensitive to any potential bias, which could be introduced by external information, i.e., source properties of a reference that is obtained separately from other methods for calibration. This is mainly because of the fact that we utilize an analytical expression of physical model involving source, and path related parameters to describe the scattering process. Moreover the type of optimization during joint inversion enables the

estimates for source parameters of relatively small sized events compared to the one used in coda-normalization methods.

2. Regional Setting and Data

Present tectonic setting of Anatolia and surrounding regions have been mainly outcome of the northward converging movements among Africa, Arab, and Eurasian plates. To the west subducting African plate with a slab roll-back dynamics beneath Anatolia along Hellenic Trench has led to back-arc extension in the Aegean and western Anatolia while compressional deformation to the east around the Bitlis–Zagros suture was explained by collisional tectonics (e.g. Taymaz et al., 1990; Bozkurt, 2001) (Fig. 1). ~~Westward extrusion of Anatolian plate controlled by these plate motions, in consequence, has been accommodated through two conjugate strike-slip fault zones separating the Anatolian and Arabian from Eurasian plates: 1600 km long east-west striking transform plate boundary, North Anatolian fault zone (NAFZ), and northeast-southwest striking East Anatolian fault zone (EAFZ) (Fig. 1). These neotectonic features could have easily traced the weakness zones along the boundaries of amalgamated continental fragments that have developed following the closure of Tethys Ocean (Şengör et al., 2005).~~

Central Anatolia is located between extensional regime to the west due to the subduction and compressional regime tectonics to the east due to the collisional tectonics. ~~There are several fault systems responsible for ongoing seismic activity in the region.~~ The major fault zone ~~in the region~~, the Central Anatolian Fault Zone (CAFZ) (Fig. 2), which primarily represents a

transtensional fault structure with small amount of left-lateral offset during the Miocene (e.g. Koçyiğit and Beyhan, 1998), can be considered as a boundary between the carbonate nappes of the Anatolide-Tauride block from the highly deformed and metamorphosed rocks in the Kırşehir block. ~~However recent studies that have reported significant lateral variations in seismic wave speeds (e.g. Fichtner et al., 2013a,b; Delph et al., 2015) and Bouguer gravity (Ateş et al., 1999) across the fault implied that a progressive relative movement along the faults would result in sharp difference in crust and mantle structures. New findings on structural, geomorphic, and geochronologic data collected from several segments along the CAFZ were interpreted that the transtensional type deformation has reactivated paleotectonic structures and finally accommodated E-W extension due to the westward extrusion of Anatolia (Higgins et al., 2015).~~ To the northwest of the CAFZ, Tuz Gölü Fault Zone (TGFZ) (Fig. 2), which is characterized by a right-lateral strike slip motion with a significant oblique-slip normal component, appears to be collocated with Tuz Gölü Basin sedimentary deposits as well as crystalline rocks within Kırşehir Block (e.g. Çemen et al., 1999; Bozkurt et al., 2001; Taymaz et al., 2004; Çubuk et al., 2014). ~~Present day crustal deformation and state of stress related to the TGFZ have been reported in Çubuk et al. (2014) via observed earthquake cluster activity reaching depths of 5-6 km with magnitudes up to M_L 5.6 in the Bala region (between 2005 and 2007) located at the north of the TGFZ (Çubuk et al., 2014).~~ At the southwest tip of the study region, the EAFZ generates large seismic activity that can be identified rather complicated seismotectonic setting: predominantly left-lateral strike-slip motion correlated well with the regional deformation pattern but also existing local clusters of thrust and normal faulting events on NS- and EW-trending subsidiary faults, respectively (Bulut et al., 2012). Such complicated behavior explains kinematic models of the shear deformation zone evolution. ~~This active left lateral fault zone since the late Miocene-Pliocene exhibits ~20 km-wide shear deformation zone with an annual 6-10 mm/yr slip rate.~~ It connects to the NAFZ at

the Karliova Triple Junction (Bozkurt, 2001) and to the south splits into various segments nearby the Adana Basin (Kaymakci et al., 2006) (Fig. 2). Toward the south, the EAFZ reaches the Dead Sea Fault Zone (DSFZ) that has a key role in accommodating northward relative motions of Arabian and African Plates with respect to Eurasia.

The present work utilizes three-component waveforms of local seismic activity detected at 72 broadband seismic stations (Fig. 2) that have been operated for 2 years between 2013 and 2015 within the framework of a temporary passive seismic experiment, the Continental Dynamics–Central Anatolian Tectonics (CD-CAT) (Portner et al., 2018). We benefit from revisited standard earthquake catalogue information (publicly available at <http://www.koeri.boun.edu.tr>) to extract waveform data for a total of 2231 examined events with station-event pair distance less than 120 km and focal depths less than 10 km. Most of the detected seismic activity in the study area is associated to several fault zones in the region, i.e., the EAFZ, CAFZ, DSFZ, TGFZ, etc. Here we note that selection of only local earthquakes is to exclude possible biases, which may be introduced by Moho boundary guided Sn-waves while upper crustal earthquakes are preferred in this study to exclude effect of relatively large-scale heterogeneities on coda wave trains. Finally a visual inspection conducted over all waveforms to ensure high-quality waveforms reduces our event number to 1193. Selected station and event distributions can be seen in Figure 2.

Observed waveforms were prepared at 5 different frequency bands with central frequencies at 0.75, 1.5, 3.0, 6.0, 12.0 Hz via a Butterworth band-pass filtering process. In the next step, we applied Hilbert transform to filtered waveform data in order to obtain the total energy envelopes. An average crustal velocity model was used to predict P and S wave onsets on envelopes and then based on this information: (i) the noise level prior to the P-wave onset was

eliminated (ii) S-wave window was determined starting at 3s prior to and 7 s afterwards S-wave onset as this allowed to include all direct S-wave energy, (iii) starting at the end of the S-wave window, a coda window of 100s at maximum was determined. Length of coda windows can be shorter when signal-to-noise ratio (SNR) is less than 2.5 or when the same window consists of coda waves from two earthquakes, which can give rise to a decline in the envelope. We omit the earthquakes with less than 10 s of coda length from our database.

3. Method

We adopted an inversion procedure that was originally developed by Sens-Schönfelder and Wegler (2006) and later modified by Eulenfeld and Wegler (2016). The forward part, which involves calculation of energy density for a specific frequency band caused by an isotropic source, is expressed in Sens-Schönfelder and Wegler (2006) as follows:

$$E_{mod}(t, r) = WR(r)G(t, r, g)e^{-bt} \quad (1)$$

where W gives source term and it is frequency dependent. $R(r)$ indicates the energy site amplification factor and b is intrinsic attenuation parameter. $G(t, r, g)$ represents Green's function that includes scattered wave field as well as direct wave and its expression is given by Paasschens (1997) as follows:

$$G(t, r, g) = e^{(-v_0 t g_0)} \left[\frac{\delta(r - v_0 t)}{4\pi r^2} + \left(\frac{4\pi v_0}{3g_0} \right)^{-\frac{3}{2}} t^{-\frac{3}{2}} \times \left(1 - \frac{r^2}{v_0^2 t^2} \right)^{\frac{1}{8}} K \left(v_0 t g_0 \left(1 - \frac{r^2}{v_0^2 t^2} \right)^{\frac{3}{4}} \right) H(v_0 t - r) \right] \quad (2)$$

Here the term within Dirac delta function represents direct wave and other term indicates scattered waves. v_0 describes the mean S-wave velocity while g_0 is the scattering coefficient.

Possible discrepancy between predicted (Eq. 1) and observed energy densities for each event at each station with N_{ij} time samples (index k) in a specific frequency band can be minimized using:

$$\epsilon(g) = \sum_{i,j,k}^{N_S, N_E, N_{ij}} (\ln E_{ijk}^{obs} - \ln E_{ijk}^{mod}(g))^2 \quad (23)$$

Here, the number of stations (index i) and events (index j) are shown by N_S and N_E , respectively. Optimization of g will be achieved when

$$\ln E_{ijk}^{obs} = \ln E_{ijk}^{mod} \quad (34) \quad \text{or}$$

$$\ln E_{ijk}^{obs} = \ln G t_{ijk}, r_{ijk}, g + \ln R_i + \ln W_j - b t_{ijk} \quad (5)$$

Equation 5 simply define an overdetermined inversion problem with $\sum_{i,j} N_{ij}$ number equation systems and with $N_S + N_E + 1$ variables and thus b , R_i , and W_j can be solved via a least-squares technique. $\epsilon(g)$ can be defined as sum over the squared residuals of the solution.

Eulenfeld and Wegler (2016) present a simple recipe to perform inversion:

(i) Calculate Green's functions through the analytic approximation of the solution for 3-D isotropic radiative transfer (e.g. Paasschens 1997; Sens-Schönfelder and Wegler, 2006) by using fixed scattering parameters and minimize equation 5 to solve for b , R_i , and W_j via a weighted least-squares approach.

(ii) Calculate $\epsilon(g)$ using equation 23.

(iii) Repeat (i) and (ii) by selecting different g to find the optimal parameters g, b, R_i and W_j

that finally minimize the error function ϵ .

In Fig. 3 an example for the minimization process that was applied at five different frequency bands is displayed for one selected event at recorded stations of the CD-CAT project.

Minimization described above for different frequencies will yield unknown spectral source energy term, W_j as well as site response, R_i and attenuation parameters, b , and g that will satisfy optimal fitting between observed and predicted coda wave envelopes. Example for this fitting can be seen in Figure 4. The present study deals with frequency dependency of W_j since this information can be later useful to obtain source displacement spectrum and thus seismic moment and moment magnitudes of analyzed earthquakes using the formula of the S-wave source displacement spectrum for a double-couple source in the far-field, which is given by Sato et al. (2012):

$$\omega M(f) = \sqrt{\frac{5\rho_0 v_0^5 W}{2\pi f^2}} \quad (56)$$

The relation between the obtained source displacement spectrum and seismic moment value was earlier described in Abercrombie (1995) by:

$$\omega M(f) = M_0 \left(1 + \left(\frac{f}{f_c} \right)^{\gamma n} \right)^{-\frac{1}{\gamma}} \quad (67)$$

where n is related to the high-frequency fall-off and γ is known as shape parameter that controls the sharpness of spectrum at corner frequency between the constant level M_0 (low frequency part) and the fall-off with f^{-n} (high frequency part). Taking logarithm of equation 67 gives:

$$\ln \omega M(f) = \ln M_0 - \frac{1}{\gamma} \ln \left(1 + \left(\frac{f}{f_c} \right)^{\gamma c} \right) \quad (78)$$

Eq. 78 describes an optimization problem of which data forms observed source displacement spectrum and four source parameters, M_0 , γ , n , and f_c are the unknown model parameters that can be resolved in a simultaneous least-squares inversion of the equation 78. Finally moment magnitude, M_w can be calculated from modeled source parameters, seismic moment, M_0 using a formula given by Hanks and Kanamori (1979):

$$M_w = \frac{2}{3} \log_{10} M_0 - 6.07 \quad (89)$$

4. Results and Discussions

4.1 Coda wave source spectra

Figure 5 displays observed values of source spectra established by inserting inverted spectral source energy term W at each frequency in Eq. 56 for all analyzed events. Each curve in this figure represents model spectrum estimate based on inversion procedure described in previous section. Modeled spectrum characteristics computed for 487 local earthquakes of which lateral distribution is presented in Figure 2 suggest, in general, that we were able to obtain typically expected source displacement spectrum with a flat region around the low frequency limit and decaying behaviour above a corner frequency.

Owing to the multiple-scattering process within small scale heterogeneities that makes coda waves gain an averaging nature, the variation in coda amplitudes due to differences source radiation pattern and path effect are reduced (Walter et al., 1995; Mayeda et al., 2003). Eulenfeld and Wegler (2016) found that radiation pattern would have only a minor influence on the S-wave coda while it might disturb attenuation models inferred from the direct S-wave

analyses unless the station distribution relative to the earthquakes indicates a good azimuthal coverage. A peak-like source function assumption for small earthquakes that are utilized in the present work was earlier proven to be adequate in early application of the coda-wave fitting studies (e.g. Sens-Schönfelder and Wegler, 2006; Gaebler et al., 2015; and Eulenfeld and Wegler, 2016).

Conventional approaches (e.g. Abercrombie, 1995; Kwiitek et al., 2011) to estimate source parameters such as corner frequency, seismic moment, high-frequency fall-off through fitting of observed displacement spectra observed at a given station in an inversion scheme could be misleading since these methods usually: (i) assume a constant value of attenuation effect (no frequency variation) defined by a factor $\exp(-\pi f t Q^{-1})$ over the spectrum, (ii) and assume omega-square model with a constant high-frequency fall-off parameter, $n=2$. Following Sens-Schönfelder and Wegler (2006) and Eulenfeld and Wegler (2016), however, we estimate attenuation parameters (intrinsic and scattering) separately within a simultaneous inversion procedure in which high-frequency fall-off parameter varies. This is fairly consistent with early studies (e.g. Ambeh and Fairhead, 1991; Eulenfeld and Wegler, 2016) where significant deviations from the omega square model ($n>3$) were reported implying that the omega-square model as a source model for small earthquakes must be reconsidered in its general acceptance. Earlier it has been well-observed that the source spectra, especially, for large earthquakes could be better explained by models of two corner frequencies (e.g., Papageorgiou and Aki, 1983; Joyner, 1984; Atkinson, 1990). Recently, Denolle et al. (2016) observed that conventional spectral model of a single-corner frequency and high-frequency fall-off rate could not explain P wave source spectra of 942 thrust earthquakes of magnitude Mw 5.5 and above. Instead, they suggested the double-corner-frequency model for large global thrust earthquakes with a lower corner frequency related to source duration and with an

upper corner frequency suggesting a shorter time scale unrelated to source duration, which exhibits its own scaling relation. Uchide and Imanishi (2016) reported similar differences from the omega-square model would be valid also for smaller earthquakes by using spectral ratio technique that involves empirical Green's function (EGF) events to avoid having a complete knowledge of path and site effects for shallow target earthquakes (M_W 3.2–4.0) in Japan. The source spectra for many of the target events in their study suggested a remarkable discrepancy from the omega-square model for relatively small earthquakes. They explained such differences by incoherent rupture due to heterogeneities in fault properties and applied stress, the double-corner-frequency model, and possibility of a high-frequency falloff exponent value slightly higher than 2. In our case, the smallest event was with M_W -coda larger than 2.0, thus we had no chance to make a similar comparison, however, high-frequency fall-off parameters varied from $n=0.5$ to $n=4$. A notable observation in the distribution of n was $n=2$ or $n=2.5$ would be better explained for earthquakes with M_W -coda >4.0 whereas the smaller magnitudes exhibited more scattered pattern of variation in n (Figure 7). Eulenfeld and Wegler (2016) claimed that the use of separate estimates of the attenuation or correction for path effect via empirically determined Green's function would be better strategy in order to invert station displacement spectra for source parameters. This is mainly because smaller earthquakes (with $n>2$), in particular, assuming omega-square model can distort the estimates of corner frequency and even seismic moment especially in regions where Q is strongly frequency dependent.

4.2 Coda wave –derived magnitude vs. M_L catalogue magnitude

A scatter plot between catalogue magnitudes based on local magnitudes (M_L) and our coda-derived magnitudes (M_W -coda) that are inferred from resultant frequency dependent source displacement spectra and thus seismic moment (e.g. Eq. 89) is shown in Fig. 6. Such

comparison suggests an overall coherency between both types of magnitudes. This implies very simple model of a first-order approximation for S-wave scattering with isotropic acoustic radiative transfer approach can be efficient to link the amplitude and decaying character of coda wave envelopes to the seismic moment of the source.

In the present study, a linear regression analyses performed between M_W -coda and M_L magnitudes (Fig. 5) resulted in an empirical formula that can be employed to convert local magnitudes into coda-derived moment magnitude calculation of local earthquakes in this region:

$$M_{W-coda} = 1.1655 \pm 0.0337 \times M_L - 0.7085 \pm 0.0128 \quad (910)$$

Bakun and Lindh (1977) empirically described the linear log seismic moment-local magnitude relation between seismic moments (M_0) and local magnitudes (M_L) for earthquakes near Oroville, California. Beside this several other studies investigated to find an optimum relation between M_W and M_L by implementing linear and/or non-linear curve-fitting approaches. Malagnini and Munafò proposed two different linear fits separated by a crossover $M_L=4.31$ could represent M_L - M_W data points obtained from earthquakes of the central and northern Apennines, Italy. Several coefficient of regression analyses in their fits account for the combined effects of source scaling and crustal attenuation as well as regional attenuation, focal depth, and rigidity at source. Goertz-Allmann et al. (2011), for instance, introduced hybrid type of scaling relation that is linear below M_L 2 and above M_L 4 and a quadratic relation in between ($2 \leq M_L \leq 4$) for earthquakes in Switzerland detected between 1998 and 2009. Edwards and Rietbrock (2009) employed a second-order polynomial equation to relate local magnitudes routinely reported in the Japan Meteorological Agency (JMA) magnitude

and moment magnitude. More recently, using multiple spectral ratio analyses Uchide and Imanishi (2018) estimated relative moment magnitudes for the Fukushima Hamadori and the northern Ibaraki prefecture areas of Japan and reported a quadratic form of correlation between JMA magnitudes and moment magnitudes. Resultant empirical curve in Uchide and Imanishi (2018) implied a considerable discrepancy between the moment magnitudes and the JMA magnitudes, with a slope of 1/2 for microearthquakes suggesting possible biases introduced by anelastic attenuation and the recording by a finite sampling interval.

Apparent move-out in Fig. 5 and Eq. 910, presumably stems from the use of different magnitude scales for comparison. Conventional magnitudes scales such as M_L , m_b inferred from phase amplitude measurements are seemingly sensitive to attenuation and 2D variation along the path (Pasyanos et al., 2016). Unlike local magnitude scales, seismic moment-based moment magnitude (M_W) essentially represents a direct measure of the strength of an earthquake caused by fault slip and is estimated from relatively flat portion of source spectra at lower frequencies that can be less sensitive to the near surface attenuation effects. The consistency between coda-derived moment magnitude and local magnitude scales for the earthquakes with M_W -coda > 3.0 indicates that our non-empirical approach successfully worked in this tectonically complex region. This observation is anticipated, for relatively large earthquakes, since more energy will be characteristic at lower frequencies. We observed similar type of consistency in early studies that investigate source properties of local and regional earthquakes based on empirical coda methods with simple 1-D radially symmetric path correction (e.g. Eken et al., 2004; Gök et al., 2016). Coda waves-derived source parameters were obtained with high-precision in Mayeda et al. (2005), Phillips et al. (2014), Pasyanos et al. (2016) following the use of 2-D path-corrected station techniques to consider the amplitude-distance relationships. Observable outliers in Figure 5, for the events

with less than M_w 3.5, however, can be attributed to the either possible biases on local magnitude values taken from the catalogue or small biases on our intrinsic (Q_i^{-1}) and scattering (Q_s^{-1}) attenuation terms. One another possible contribution to such mismatch might be associated to the influences of mode conversions between body and surface waves or surface-to-surface wave scattering (e.g. Wu & Aki 1985) that are not restricted to low frequencies ($<1\text{Hz}$) (Sens-Schönfelder and Wegler, 2006).

5. Conclusions

This study provides an independent solution for estimating seismic source parameters such as seismic moment and moment magnitude for local earthquakes in central Anatolia without requiring *a priori* information on reference events with waveform modelling results to be used for calibration or *a priori* information on attenuation for path effect corrections. In this regard, the approach used here can be easy and useful tool for investigation of source properties of local events detected at temporal seismic networks. Moreover, seismic moment can be approximated via waveform modelling methods but due to the small-scale heterogeneities of the media that waves propagate, it is often a hard task to establish Green's function for small earthquakes ($M_L < 3.5$). An analytical expression of energy density Green's function in a statistical manner employed in the present work enables neglecting the interaction of the small-scale inhomogeneities with seismic waves as this can be practical for seismic moment calculations of small events that may pose source energy at high-frequency. It is noteworthy to mention that our isotropic scattering assumption does not consider anisotropic case, which could be valid for real media, but still provides a simple and effective tool to define the transport for the anisotropic case since the estimated scattering coefficient

can be interpreted as transport scattering coefficient. An averaging over S-wave window enables to overcome biases caused by using unrealistic Green's function (Gaebler *et al.* 2015). Since the present study mainly focuses on source properties of local earthquakes in the study area, scattering and intrinsic attenuation properties that are other products of our coda envelope fitting procedure will be examined in details within a future work. Finally, the empirical relation developed between M_W -coda and M_L will be a useful tool for quickly converting catalogue magnitudes to moment magnitudes for local earthquakes in the study area.

Data and resources

The python code used for carrying out the inverse modeling is available under the permissive MIT license and is distributed at <https://github.com/trichter/qopen>. We are grateful to the IRIS Data Management Center for maintaining, archiving and making the continuous broadband data used in this study open to the international scientific community.

Acknowledgement

The facilities of IRIS Data Services, and specifically the IRIS Data Management Center, were used for access to waveforms, related metadata, and/or derived products used in this study. IRIS Data Services are funded through the Seismological Facilities for the Advancement of Geoscience and EarthScope (SAGE) Proposal of the National Science Foundation under Cooperative Agreement EAR-1261681. Data for the CD-CAT experiment (https://doi.org/10.7914/SN/YB_2013) are available from the IRIS Data Management Center at <http://www.iris.edu/hq/>. Tuna Eken acknowledge financial support from Alexander von Humboldt Foundation (AvH) towards computational and peripherals resources. **I am grateful to the Topical Editor Charlotte Krawczyk for handling the revision process and Takahiko**

413 Uchide for his valuable opinions on the improvement of manuscript.

414

415

416 *References*

417 Abercrombie, R.E.: Earthquake source scaling relationships from -1 to 5 ML using
418 seismograms recorded at 2.5-km depth, J. geophys. Res., 100(B12), 24 015–24 036,
419 1995.

420 Aki, K., and Chouet., B.: Origin of coda waves: Source, attenuation, and scattering effects, J.
421 Geophys. Res. 80, 3322–3342, 1975.

422 ~~Ates, A., Kearey, P., and Tufan, S.: New gravity and magnetic anomaly maps of Turkey:~~
423 ~~Geophysical Journal International, v. 136, p. 499–502, 1999.~~

424 Atkinson, G. M.: A comparison of eastern North American ground motion observations with
425 theoretical predictions, Seismol. Res. Lett. 61, 171–180, 1990.

426 Bakun, W.H. and Lindh, A.G.: Local Magnitudes, Seismic Moments, and Coda Durations for
427 Earthquakes Near Oroville, California, Bulletin of the
428 Seismological Society of America. Vol.67, No.3, pp. 615–629, 1977.

429 Bozkurt, E.: Neotectonics of Turkey—A synthesis: Geodinamica Acta, v. 14, p. 3–30, 2001.

430 Bulut, F., Bohnhoff, M., Eken, T., Janssen, C., Kılıç, T., and Dresen, G.: The East Anatolian
431 fault zone: Seismotectonic setting and spatiotemporal characteristics of seismicity based
432 on precise earthquake locations: Journal of Geophysical Research, v. 117, B07304,
433 <https://doi.org/10.1029/2011JB008966>, 2012.

434 Çemen, I., Göncüoğlu, M.C., and Dirik, K.: Structural evolution of the Tuz Gölü basin in central
435 Anatolia, Turkey: Journal of Geology, v. 107, p. 693–706, <https://doi.org/10.1086/314379>, 1999.

437 Çubuk Y, Yolsal-Çevikbilen S, Taymaz, T.: Source parameters of the 20052008 Bal^aSirapinar
 438 (central Turkey) earthquakes: Implications for the internal deformation of the Anatolian
 439 plate. *Tectonophysics* 635(Supplement C) :125 – 153, 2014.

440 ~~Delph, J.R., Biryol, C.B., Beek, S.L., Zandt, G., and Ward, K.M.: Shear wave velocity structure~~
 441 ~~of the Anatolian plate: Anomalous slow crust in southwestern Turkey: Geophysical~~
 442 ~~Journal International, v. 202, p. 261–276, 2015.~~

443 Denolle, M. A., and Shearer, P.M.: New perspectives on self-similarity for shallow thrust
 444 earthquakes, *J. Geophys. Res. Solid Earth*, 121, 6533–6565, 2016.

445 Edwards, B., & Rietbrock, A.: A comparative study on attenuation and source-scaling relations
 446 in the Kantō, Tokai, and Chubu regions of Japan, using data from Hi-net and KiK-net.
 447 *Bulletin of the Seismological Society of America*, 99, 2435–2460, 2009.

448 Eken, T., Mayeda, K., Hofstetter, A., Gök, R., Orgülü, G. and Turkelli, N.: An application of the
 449 coda methodology for moment-rate spectra using broadband stations in Turkey.
 450 *Geophys. Res. Lett.*, 31, L11609, 2004.

451 Eulenfeld, T. and Wegler, U.: Measurement of intrinsic and scattering attenuation of shear
 452 waves in two sedimentary basins and comparison to crystalline sites in Germany,
 453 *Geophys J Int.*, 205(2):744-757, 2016.

454 Eulenfeld, T. and Wegler, U.: Crustal intrinsic and scattering attenuation of high-frequency
 455 shear waves in the contiguous United States. *J Geophys., Res*, 122, 2017.

456 Favreau, P., and Archuleta, R.J.: Direct seismic energy modelling and application to the 1979
 457 Imperial Valley earthquake, *Geophys. Res. Lett.*, 30, 1198, 2003.

458 ~~Fichtner, A., Saygin, E., Taymaz, T., Cupillard, P., Capdeville, Y., and Trampert, J.: The deep~~
 459 ~~structure of the North Anatolian Fault Zone, *Earth Planet. Sc. Lett.*, 373, 109–117,~~
 460 ~~2013a.~~

461 ~~Fichtner, A., Trampert, J., Cupillard, P., Saygin, E., Taymaz, T., Capdeville, Y., and Villasenor,~~
 462 ~~A.: Multiscale full waveform inversion, Geophys. J. Int., 194, 534–556,~~
 463 ~~doi:10.1093/gji/ggt118, 2013b.~~
 464 Gaebler, P.J., Eulenfeld, T. & Wegler, U.: Seismic scattering and absorption parameters in the
 465 W-Bohemia/Vogtland region from elastic and acoustic radiative transfer theory,
 466 Geophys. J. Int., 203(3), 1471–1481, 2015.
 467 Gaebler, P.J., Eken, T., Bektaş, H.Ö, Eulenfeld, T., Wegler, U., Taymaz, T.: Imaging of Shear
 468 Wave Attenuation Along the Central Part of the North Anatolian Fault Zone, Turkey,
 469 submitted to the Journal of Seismology, 2018.
 470 Goertz-Allmann, B. P., Edwards, B., Bethmann, F., Deichmann, N., Clinton, J., Fäh, D., &
 471 Giardini, D.: A new empirical magnitude scaling relation for Switzerland. Bulletin of the
 472 Seismological Society of America, 101, 3088–3095, 2011.
 473 Gök, R., Kaviani, A., Matzel, E. M., Pasyanos, M. E., Mayeda, K., Yetirmishli, G., El-Hussain,
 474 I., Al-Amri, A., Al-Jeri, F., Godoladze, T., Kalafat, D., Sandvol, E. A., and Walter,
 475 W.R.: Moment Magnitudes of Local/Regional Events from 1D Coda Calibrations in the
 476 Broader Middle East Region. Bull Seismol Soc Am., 106(5):1926-1938, 2016.
 477 Gusev, A.A. & Abubakirov, I.R.: Simulated envelopes of non-isotropically scattered body
 478 waves as compared to observed ones: another manifestation of fractal heterogeneity,
 479 Geophys. J. Int., 127(1), 49–60, 1996.
 480 Hanks, T.C. and Kanamori, H.: A moment magnitude scale, J. Geophys., Res., 84, 2348–2350,
 481 1979.
 482 ~~Higgins, M., Schoenbohm, L.M., Brocard, G., Kaymakci, N., Gosse, J.C., and Cosca, M.A.:~~
 483 ~~New kinematic and geochronologic evidence for the Quaternary evolution of the Central~~
 484 ~~Anatolian fault zone (CAFZ), Tectonics, v. 34, pages, 2118–2141, 2015.~~

485 Izgi, G., Eken, T., Gaebler, P., and Taymaz, T.: Frequency-Dependent Shear Wave Attenuation
 486 Along the Western Part of the North Anatolian Fault Zone, Geophysical Research
 487 Abstracts, Vol. 20, EGU2018-629-2, 2018.

488 Kaymakci, N. Inceöz, M. Ertepinar, P.: 3D architecture and Neogene evolution of the Malatya
 489 Basin: inferences for the kinematics of the Malatya and Ovacik Fault Zones. Turkish
 490 Journal of Earth Sciences, 15, 123-154, 2006.

491 Kwiatek, G., Plenkers, K. & Dresen, G.: 2011. Source parameters of pico-seismicity recorded at
 492 Mponeng Deep Gold Mine, South Africa: implications for scaling relations, Bull. seism.
 493 Soc. Am., 101(6), 2592–2608, 2011.

494 Malagnini, L., Mayeda, K., Akinci, A., and Bragato, P. L.: Estimating absolute site effects,
 495 Bull. Seismol. Soc. Am. 94, no. 4, 1343–1352, 2004.

496 Malagnini, L., and Munafò, I.: On the Relationship between M_L and M_w in a Broad Range: An
 497 Example from the Apennines, Italy, Bulletin of the Seismological Society of America,
 498 Vol. 108, No. 2, pp. 1018–1024, 2018.

499 Mayeda, K., and Walter, W.R.: Moment, energy, stress drop, and source spectra of western
 500 United States earthquakes from regional coda envelopes, J. Geophys. Res. 101, 11,195–
 501 11,208, 1996.

502 Mayeda, K., Hofstetter, A., O’Boyle, J.L., and Walter, W.R.: Stable and transportable regional
 503 magnitudes based on coda-derived moment-rate spectra, Bull. Seismol. Soc. Am. 93,
 504 224–239: 2003.

505 Mayeda, K., Malagnini, L., Phillips, W. S., Walter, W. R., and Dreger, D.: 2D or not 2D, that is
 506 the question: A Northern California Test. Geophys- ical Research Letters, 32(12), 2005.

507 Morasca, P., Mayeda, K., Malagnini, L. and Walter, W.R.: Coda and direct-wave attenuation
 508 tomography in northern Italy, Bull Seismol Soc Am., v. 98, pages, 1936-1946, 2004.

509 Morasca, P., Mayeda, K., Gök, R., Phillips, W.S., and Malagnini, L.: Coda-derived source
 510 spectra, moment magnitudes and energy-moment scaling in the western Alps, *Geophys.*
 511 *J. Int.*, 160, 263–275, 2008.

512 Paasschens, J.: Solution of the time-dependent Boltzmann equation, *Phys. Rev. E*, 56(1), 1135–
 513 1141, 1997.

514 Papageorgiou, A., and Aki, K.: A specific barrier model for the quantitative description of
 515 inhomogeneous faulting and the prediction of strong ground motion I: Description of the
 516 model, *Bull. Seismol. Soc. Am.*, 73(3), 693–722, 1983.

517 Pasyanos, M. E., R. Gök, and Walter, W.R.: 2-D variations in coda amplitudes in the Middle
 518 East. *Bull. Seismol. Soc. Am.* 106, no. 5, 2016.

519 Phillips, W. S., Mayeda, K. M., and Malagnini, L.: How to invert multi-band, regional phase
 520 amplitudes for 2-d attenuation and source parameters: Tests using the usarray. *Pure and*
 521 *Applied Geophysics*, 171(3):469-484, 2014.

522 Portner, D.E., Delph, J.R., Biryol, C.B., Beck, S.L., Zandt, G., Özacar, A.A., Sandvol, E., and
 523 Türkelli, N.: Subduction termination through progressive slab deformation across
 524 Eastern Mediterranean subduction zones from updated P-wave tomography beneath
 525 Anatolia, *Geosphere*, 14(3): 907-925, 2018.

526 Przybilla, J. and Korn, M.: Monte Carlo simulation of radiative energy transfer in continuous
 527 elastic random mediathree-component envelopes and numerical validation. *Geophys J*
 528 *Int* , 173(2):566-576, 2008.

529 Rautian, T.G. & Khalturin, V.I.: The use of the coda for determination of the earthquake source
 530 spectrum, *Bull. Seism. Soc. Am.*, 68(4), 923–948, 1978.

531 Sato, H. and Fehler, M.C.: *Seismic Wave Propagation and Scattering in the Heterogeneous*
 532 *Earth*, Springer-Verlag, New York, 1998.

533 Sato, H., Fehler, M.C. & Maeda, T. Seismic Wave Propagation, and Scattering in the
534 Heterogeneous Earth, 2nd edn, Springer: 2012.

535 Sens-Schönfelder, C. and Wegler, U.: Radiative transfer theory for estimation of the seismic
536 moment. *Geophys J Int*, 167(3):1363-1372.

537 ~~Şengör, A.M.C., Tüysüz, O., İmren, C., Sakıncı, M., Eyidoğan, H., Görür, N., Le Pichon, X., and~~
538 ~~Rangin, C.: The North Anatolian fault: A new look: *Annual Review of Earth and*~~
539 ~~*Planetary Sciences*, v. 33, p. 37–112, 2005.~~

540 Taymaz, T., Jackson, J., Westaway, R.: Earthquake mechanisms in the Hellenic Trench near
541 Crete. *Geophys. J. Int.* 102, 695–731, 1990.

542 Taymaz, T., Westaway, R., Reilinger, R.: Active faulting and crustal deformation in the eastern
543 Mediterranean Region. *Spec. Issue Tectonophys.* 391 (1-4), 1–9. [http://](http://dx.doi.org/10.1016/j.tecto.2004.07.005)
544 dx.doi.org/10.1016/j.tecto.2004.07.005, 2004.

545 Uchide, T., & Imanishi, K.: Small earthquakes deviate from the omega-square model as revealed
546 by multiple spectral ratio analysis. *Bulletin of the Seismological Society of America*,
547 106(3), 1357–1363, 2016.

548 Uchide, T., & Imanishi, K.: Underestimation of microearthquake size by the magnitude scale of
549 the Japan Meteorological Agency: Influence on earthquake statistics. *Journal of*
550 *Geophysical Research: Solid Earth*, 123, 606–620, 2018.

551 Yoo, S.-H., Rhie, J., Choi, H.-S., and Mayeda, K.: Coda-derived source parameters of
552 earthquakes and their scaling relationships in the Korean Peninsula, *Bull. Seismol. Soc.*
553 *Am.*, 101, 2388–2398, 2011.

554 Wu, R. and Aki, K.: The fractal nature of the inhomogeneities in the lithosphere evidenced from
555 seismic wave scattering, *Pure appl. Geophys.*, 123(6), 805–818, 1985.

556 Zeng, Y., Su, F. and Aki, K.: Scattering wave energy propagation in a random isotropic
557 scattering medium: 1. Theory, *J. Geophys. Res.*, 96(B1), 607–619, 1991.

Figure Captions

Figure 1. Major tectonic features of Turkey and its adjacent. The plate boundary data used here is taken from Bird (2003). Subduction zones are black, continental transform faults are red, continental rift boundaries are green, and spreading ridges boundaries are yellow. NAFZ, EAFZ, and DSFZ are the North Anatolian Fault, East Anatolian Fault, and the Dead Sea fault, respectively.

Figure 2. Epicentral distribution of all local events selected from the study area in the KOERI catalogue. Gray circles represent earthquakes with poor quality that are not considered for the current study while black indicates the location of local events with good quality. Red circles among these events are 487 events used in coda wave inversion since they are successful at passing quality criteria of further pre-processing procedure.

Figure 3. An example from the inversion procedure explained in chapter 3. Here coda envelope fitting optimization is performed on band-pass filtered (8-16Hz) digital recordings of an earthquake (2014 April 09, M_w -coda3.2) extracted for 7 seismic stations that operated within the CD-CAT array. Large panel at the lower left-hand side displays the error function ϵ as a function of g_0 . Thick blue cross here represent the optimal value of $g = g_0$. Other small panels at upper and right-hand side show the least- squares solution of the weighted linear equation system for the first 6 guesses and optimal guess for g_0 . There dots and gray curves indicate the ratio between energy (E^{obs}) and the Green's function (G) obtained for direct S-

waves and observed envelopes at various stations, respectively. Please notice that during this optimization process envelopes are corrected for the obtained site corrections R_i . The slope of linear curve at each small panel yields $-b$ and while its intercept W are the intrinsic attenuation and source related terms at the right-hand side of equation 5 part of the right-hand side of the equation system.

Figure 4. a) Results of the inversion of the 2014-April-09, M_W -coda3.2 earthquake: Sample fits between observed and calculated energy densities in the frequency band 0.5–1.0 Hz are given for 6 different stations (see upper right corner for event ID, station name, and distance to hypocenter). Note that light blue curves represent observed envelope. Smoothed observed calculated envelopes in each panel are presented by blue and red curves, respectively. Blue and red dots exhibit location of the average value for observed and calculated envelopes within the S-wave window, respectively. b) The same as in (a) obtained in the frequency band 4.0–8.0 Hz.

Figure 5. All individual observed (black squares) and predicted (gray curve) source displacement spectra observed at 72 stations from 487 local earthquakes in central Anatolia.

Figure 6: Scatter plot between local magnitudes (M_L) of analyzed events with coda waves-derived magnitudes (M_W -coda) of the same events. The outcome of a linear regression analysis yielded an empirical formula (e.g. Eq. 910) to identify the overall agreement represented by gray straight line. Yellow and red dashed lines indicate upper and lower limit of linearly fitting to that scatter.

Figure 7: Same scatter plot displayed in Fig. 6 color coded by estimated high-frequency fall-off parameter for each inverted event.

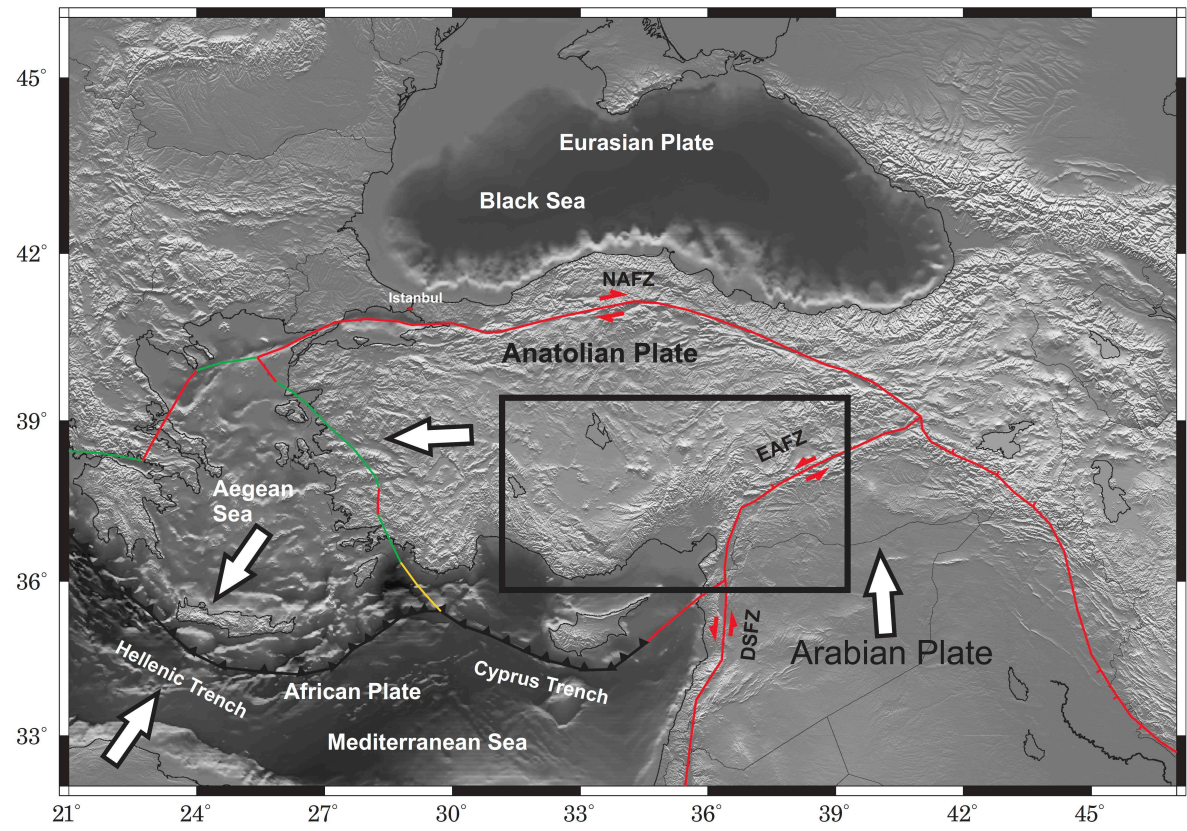


Figure 1.

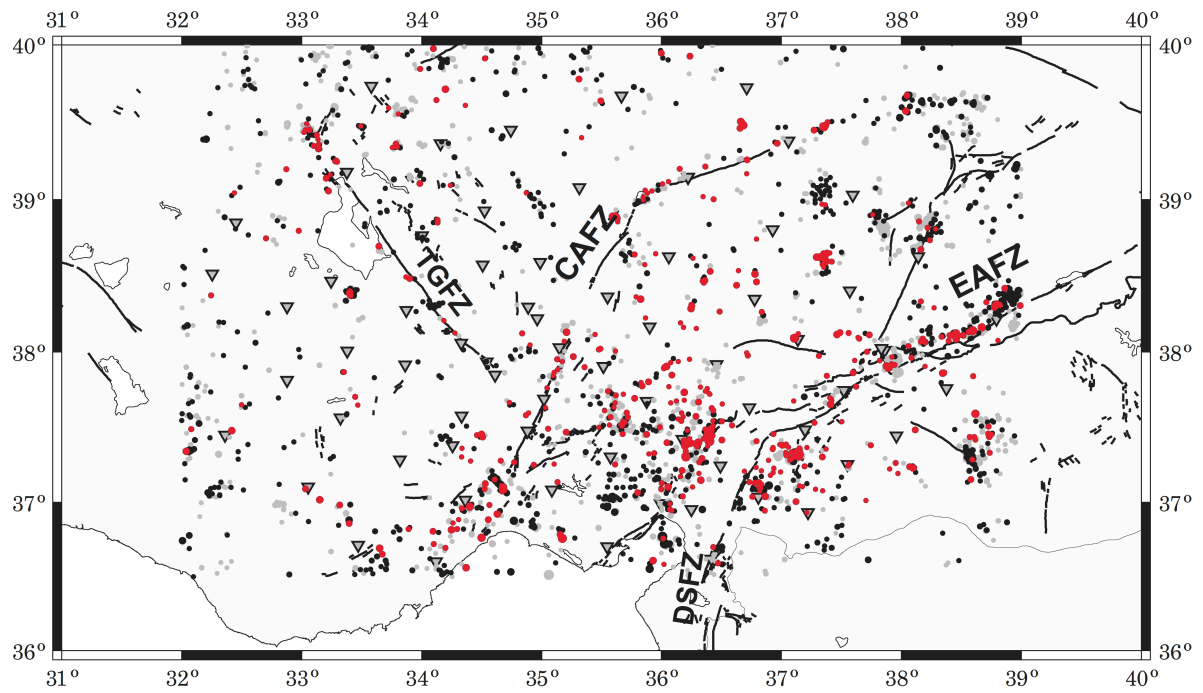


Figure 2.

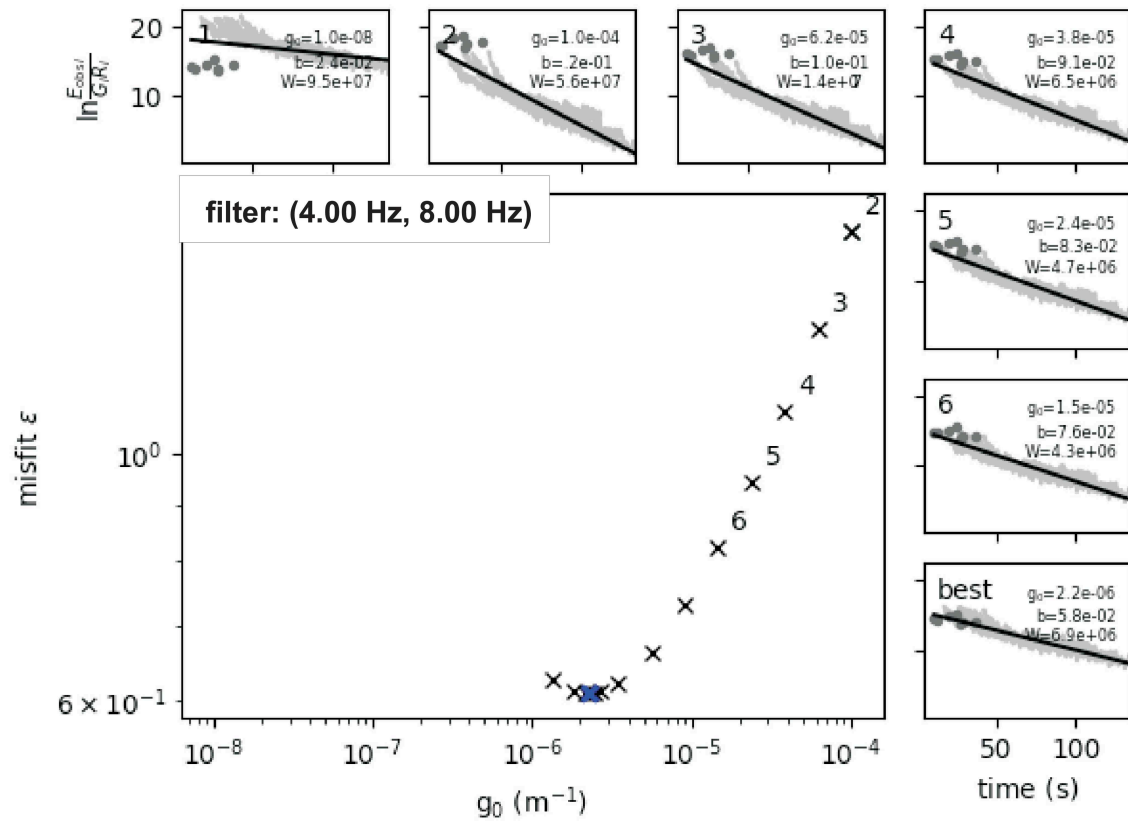


Figure 3.

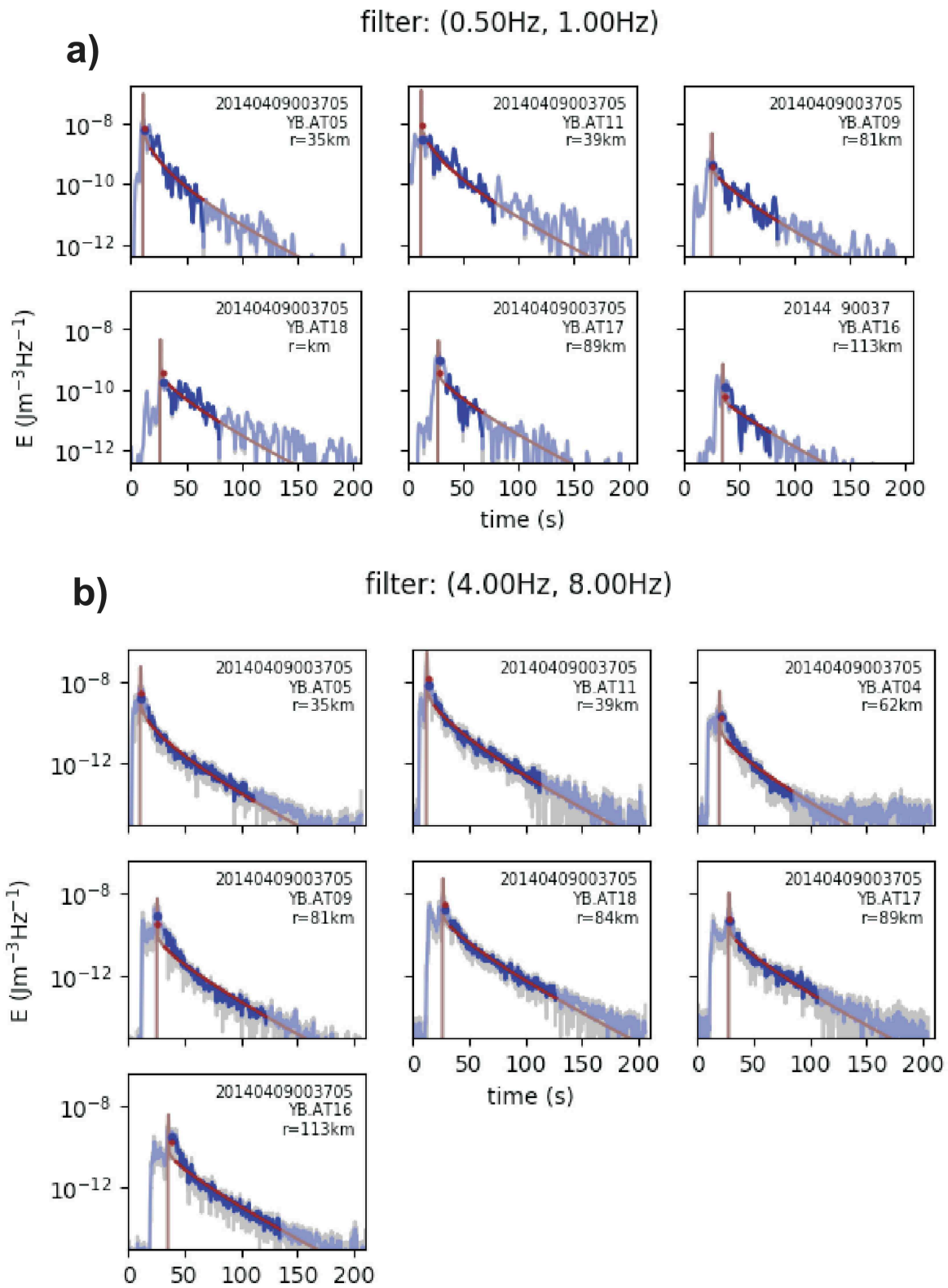
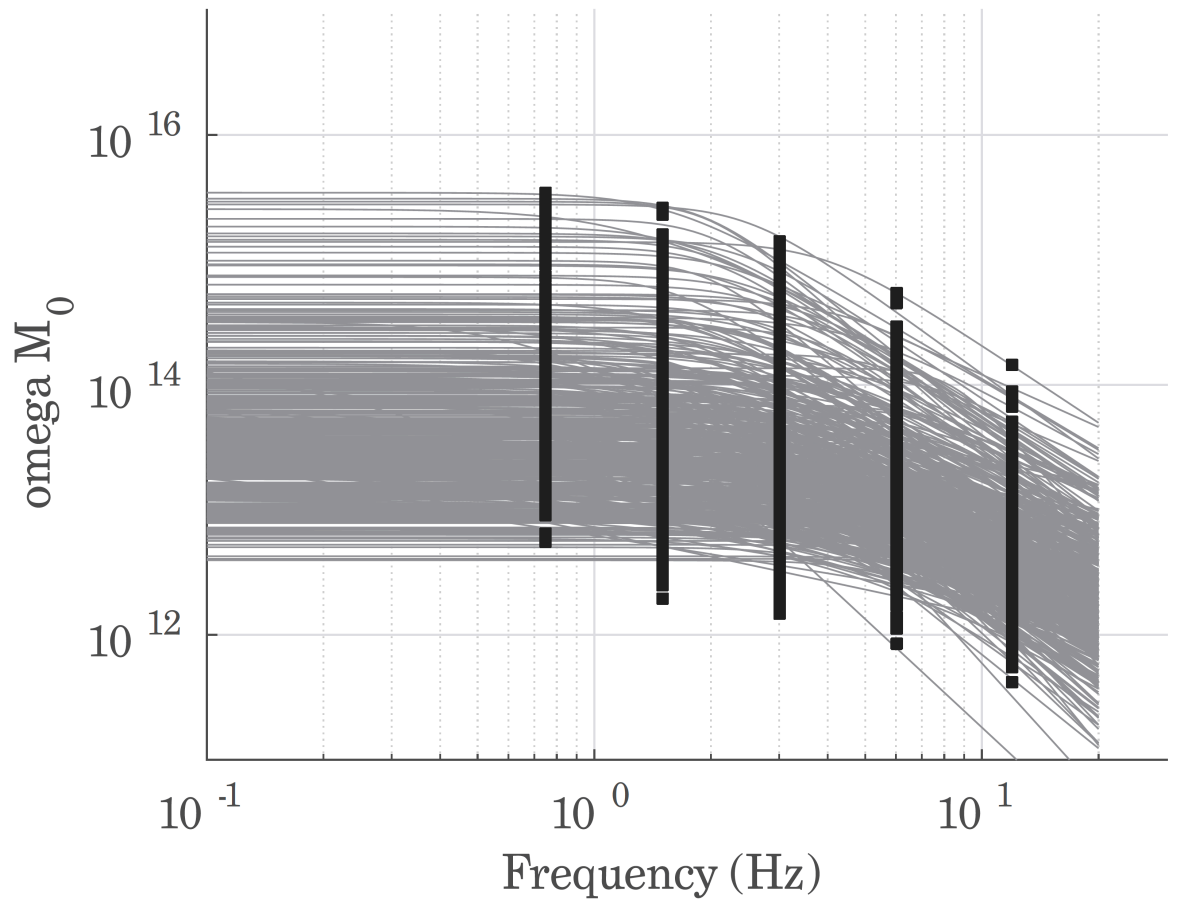


Figure 4.

651
652
653
654
655



656
657
658
659
660
661
662
663
664
665
666
667
668
669
670
671
672
673
674
675
676

Figure 5.

677
678
679
680
681
682

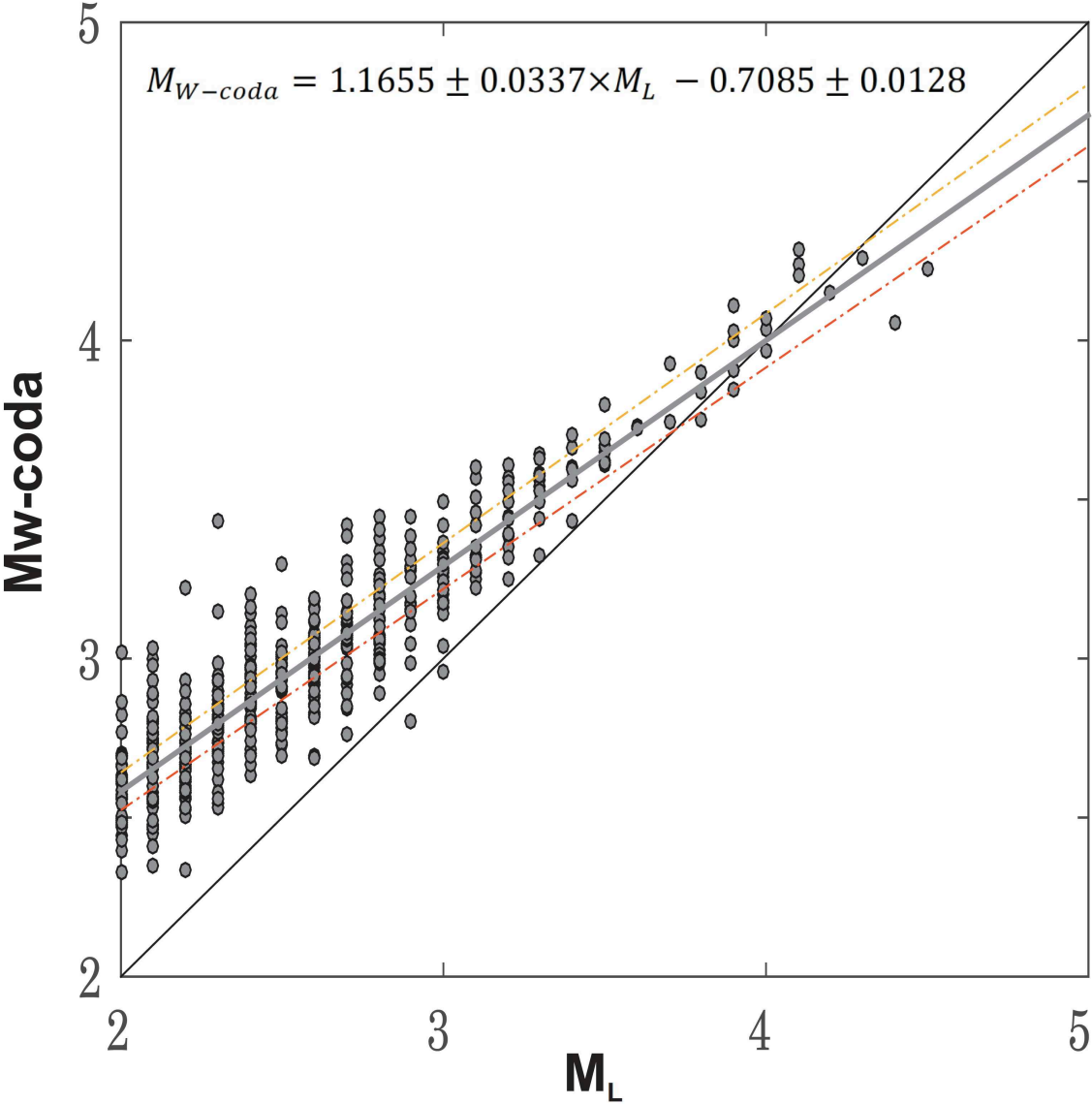
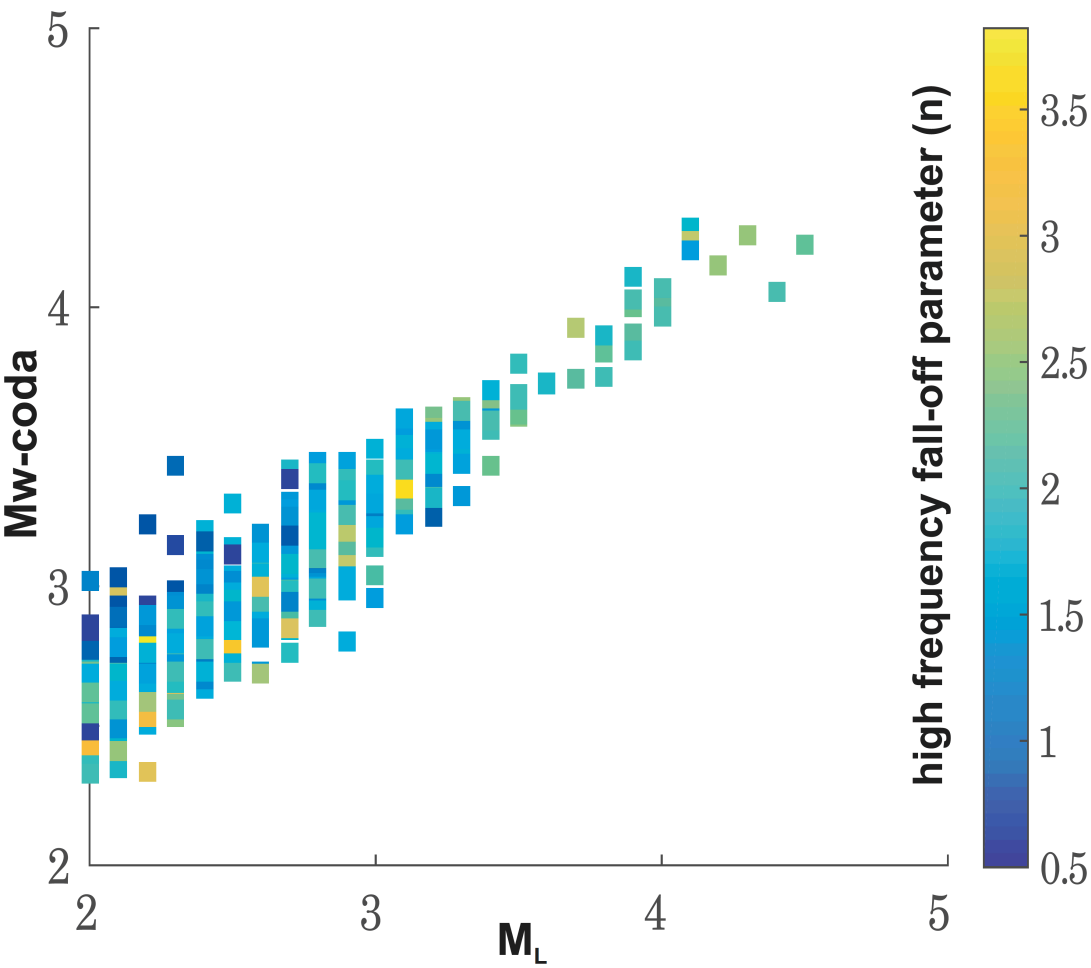


Figure 6.

683
684
685
686
687
688
689
690
691
692
693
694
695
696

697
698



699
700
701
702

Figure 7.

Moment magnitude estimates for Central Anatolian earthquakes using coda waves

Tuna Eken¹

¹*Department of Geophysical Engineering, the Faculty of Mines, Istanbul Technical University, 34469 Maslak, Sarıyer, Istanbul, Turkey*

Abstract

Proper estimate of moment magnitude that is a physical measure of the energy released at earthquake source is essential for better seismic hazard assessments in tectonically active regions. Here a coda wave modeling approach that enables the source displacement spectrum modeling of examined event was used to estimate moment magnitude of central Anatolia earthquakes. To achieve this aim, three component waveforms of local earthquakes with magnitudes $2.0 \leq M_L \leq 5.2$ recorded at 72 seismic stations which have been operated between 2013 and 2015 within the framework of the CD-CAT passive seismic experiment. An inversion on the coda wave traces of each selected single event in our database was performed in five different frequency bands between 0.75 and 12 Hz. Our resultant moment magnitudes (M_W -coda) exhibit a good agreement with routinely reported local magnitude (M_L) estimates for study area. Apparent move-out that is, particularly, significant around the scattered variation of M_L - M_W -coda data points for small earthquakes ($M_L < 3.5$) can be explained by possible biases of wrong assumptions to account for anelastic attenuation and of seismic recordings with finite sampling interval. Finally, we present an empirical relation between M_W -coda and M_L for central Anatolian earthquakes.

Keyword(s): Coda waves modelling, seismic moment, moment magnitude, Radiative Transfer Theory

1. Introduction

The robust and stable knowledge of source properties (e.g. moment magnitude estimates) is crucial in seismically active countries such as Turkey for a better evaluation of seismic hazard potential as this highly depends on establishment of reliable seismicity catalogs. Moreover, accurate information on source parameters could be important when developing regional attenuation properties.

Conventional type of magnitude scales (M_L , m_b , M_S) as the result of empirically derived using direct wave analyses can be biased due to various effects such as source radiation pattern, directivity, and heterogeneities along the path since they may cause drastic changes in direct wave amplitude measurements (e.g., Favreau and Archuleta, 2003). Instead several early studies depending on the analysis of local and/or regional coda envelopes have indicated that coda wave amplitudes are significantly less variable by a factor of 3-to-5 compared to direct wave amplitudes (e.g., Mayeda and Walter, 1996; Mayeda et al., 2003; Eken et al., 2004; Malagnini et al., 2004; Gök et al., 2016). In fact local or regional coda waves that are usually considered to be generally to be composed of scattered waves and can be simply explained by that sample the single scattering model of Aki (1969) have been proven to be virtually insensitive to any source radiation pattern effect in contrast to direct waves because of the volume averaging property of the coda waves sampling the entire focal sphere (e.g., Aki and Chouet, 1975; Rautian and Khalturin, 1978). In Sato and Fehler (1998) and Sato et al. (2012) an extensive review study on the theoretical background of coda generation and advances of empirical observations and modelling efforts can be found in details.

There have been several approaches used for extracting information on earthquake source size via coda wave analyses. These approaches can be mainly divided into two groups. The first group of studies employs coda normalization strategy in which measurements require a correction for seismic attenuation parameters (e.g. intrinsic and scattering) that can be described by some empirical quality factors. To calibrate final source properties reference events are used to adjust measurements with respect to each other. For forward generation of synthetic coda envelopes, either single-backscattering or more advanced multiple-backscattering approximation are used. An example to this group is an empirical method originally developed by Mayeda et al. (2003) to investigate seismic source parameters such as energy, moment, and apparent stress drop in the western United States and in Middle East. They corrected observed coda envelopes for various influences, for instance, path effect, S-to-coda transfer function, site effect, and any distance-dependent changes in coda envelope shape. Empirical coda envelope method have been successfully applied to different regions with complicated tectonics such as northern Italy (e.g. Morasca et al., 2008), Turkey and Middle East (e.g. Eken et al., 2004; Gök et al. 2016); or Korean Peninsula (e.g. Yoo et al., 2013).

Second type of approach is a joint inversion technique that is based on a simultaneous optimization of source, path, and site specific terms via synthetic and observed coda envelope fitting within a selected time window including observed coda and direct-S wave parts. In this approach, the Radiative Transfer Theory (RTT) is employed for analytic expression of synthetic coda wave envelopes. The method that does not rely on coda normalization strategy was originally developed by Sens-Schönfelder and Wegler (2006) and successfully tested on local and regional earthquakes ($4 \leq M_l \leq 6$) detected by the German Regional Seismic Network. Further it has been applied to investigate source and frequency dependent

attenuation properties of different geological settings, i.e., Upper Rhine Graben and Molasse Basin regions in Germany and western Bohemia/Vogtland in Czechia (Eulenfeld and Wegler, 2016); entire United States (2017); central and western North Anatolian Fault Zone (Gaebler et al., 2018; Izgi et al., 2018). A more realistic earth model in which anisotropic scattering conditions were earlier considered by Gusev and Abubakirov (1987) yielded peak broadening effects of the direct seismic wave arrivals. This approach later was used in previous studies (e.g. Zeng, 1993; Przybilla and Korn, 2008; Gaebler et al., 2015) that dealt with propagation of P-wave elastic energy and the effect of conversion between P- and S-wave energies.

In the current work I present estimated source spectra as an output of a joint inversion of S- and coda waves parts of local earthquake waveforms 487 local earthquakes with magnitudes $2.0 < ML < 4.5$ detected in central Anatolia for their source parameters. The approach used here employs isotropic acoustic RTT approach for forward calculation of synthetic coda envelopes. Gaebler et al. (2015) has observed that modeling results from isotropic scattering were almost comparable with those inferred from relatively more complex elastic RTT simulations with anisotropic scattering conditions. The use of a joint inversion technique is advantageous since it is insensitive to any potential bias, which could be introduced by external information, i.e., source properties of a reference that is obtained separately from other methods for calibration. This is mainly because of the fact that we utilize an analytical expression of physical model involving source, and path related parameters to describe the scattering process. Moreover the type of optimization during joint inversion enables the estimates for source parameters of relatively small sized events compared to the one used in coda-normalization methods.

2. Regional Setting and Data

Present tectonic setting of Anatolia and surrounding regions have been mainly outcome of the northward converging movements among Africa, Arab, and Eurasian plates. To the west subducting African plate with a slab roll-back dynamics beneath Anatolia along Hellenic Trench has led to back-arc extension in the Aegean and western Anatolia while compressional deformation to the east around the Bitlis–Zagros suture was explained by collisional tectonics (e.g. Taymaz et al., 1990; Bozkurt, 2001) (Fig. 1). Central Anatolia is located between extensional regime to the west due to the subduction and compressional regime tectonics to the east due to the collisional tectonics. There are several fault systems responsible for ongoing seismic activity in the region. The major fault zone, the Central Anatolian Fault Zone (CAFZ) (Fig. 2), which primarily represents a transtensional fault structure with small amount of left-lateral offset during the Miocene (e.g. Koçyiğit and Beyhan, 1998), can be considered as a boundary between the carbonate nappes of the Anatolide-Tauride block from the highly deformed and metamorphosed rocks in the Kırşehir block. To the northwest of the CAFZ, Tuz Gölü Fault Zone (TGFZ) (Fig. 2), which is characterized by a right-lateral strike slip motion with a significant oblique-slip normal component, appears to be collocated with Tuz Gölü Basin sedimentary deposits as well as crystalline rocks within Kırşehir Block (e.g. Çemen et al., 1999; Bozkurt et al., 2001; Taymaz et al., 2004; Çubuk et al., 2014). At the southwest tip of the study region, the EAFZ generates large seismic activity that can be identified rather complicated seismotectonic setting: predominantly left-lateral strike-slip motion correlated well with the regional deformation pattern but also existing local clusters of thrust and normal faulting events on NS- and EW-trending subsidiary faults, respectively (Bulut et al., 2012). Such complicated behavior explains kinematic models of the shear deformation zone

evolution. It connects to the NAFZ at the Karlıova Triple Junction (Bozkurt, 2001) and to the south splits into various segments nearby the Adana Basin (Kaymakci et al., 2006) (Fig. 2). Toward the south, the EAFZ reaches the Dead Sea Fault Zone (DSFZ) that has a key role in accommodating northward relative motions of Arabian and African Plates with respect to Eurasia.

The present work utilizes three-component waveforms of local seismic activity detected at 72 broadband seismic stations (Fig. 2) that have been operated for 2 years between 2013 and 2015 within the framework of a temporary passive seismic experiment, the Continental Dynamics–Central Anatolian Tectonics (CD-CAT) (Portner et al., 2018). We benefit from revisited standard earthquake catalogue information (publicly available at <http://www.koeri.boun.edu.tr>) to extract waveform data for a total of 2231 examined events with station-event pair distance less than 120 km and focal depths less than 10 km. Most of the detected seismic activity in the study area is associated to several fault zones in the region, i.e., the EAFZ, CAFZ, DSFZ, TGFZ, etc. Here we note that selection of only local earthquakes is to exclude possible biases, which may be introduced by Moho boundary guided Sn-waves while upper crustal earthquakes are preferred in this study to exclude effect of relatively large-scale heterogeneities on coda wave trains. Finally a visual inspection conducted over all waveforms to ensure high-quality waveforms reduces our event number to 1193. Selected station and event distributions can be seen in Figure 2.

Observed waveforms were prepared at 5 different frequency bands with central frequencies at 0.75, 1.5, 3.0, 6.0, 12.0 Hz via a Butterworth band-pass filtering process. In the next step, we applied Hilbert transform to filtered waveform data in order to obtain the total energy envelopes. An average crustal velocity model was used to predict P and S wave onsets on

envelopes and then based on this information: (i) the noise level prior to the P-wave onset was eliminated (ii) S-wave window was determined starting at 3s prior to and 7 s afterwards S-wave onset as this allowed to include all direct S-wave energy, (iii) starting at the end of the S-wave window, a coda window of 100s at maximum was determined. Length of coda windows can be shorter when signal-to-noise ratio (SNR) is less than 2.5 or when the same window consists of coda waves from two earthquakes, which can give rise to a decline in the envelope. We omit the earthquakes with less than 10 s of coda length from our database.

3. Method

We adopted an inversion procedure that was originally developed by Sens-Schönfelder and Wegler (2006) and later modified by Eulenfeld and Wegler (2016). The forward part, which involves calculation of energy density for a specific frequency band caused by an isotropic source, is expressed in Sens-Schönfelder and Wegler (2006) as follows:

$$E_{mod}(t, r) = WR(r)G(t, r, g)e^{-bt} \quad (1)$$

where W gives source term and it is frequency dependent. R(r) indicates the energy site amplification factor and b is intrinsic attenuation parameter. $G(t, r, g)$ represents Green's function that includes scattered wave field as well as direct wave and its expression is given by Paasschens (1997) as follows:

$$G(t, r, g) = e^{(-v_0 t g_0)} \left[\frac{\delta(r - v_0 t)}{4\pi r^2} + \left(\frac{4\pi v_0}{3g_0} \right)^{-\frac{3}{2}} t^{-\frac{3}{2}} \times \left(1 - \frac{r^2}{v_0^2 t^2} \right)^{\frac{1}{8}} K \left(v_0 t g_0 \left(1 - \frac{r^2}{v_0^2 t^2} \right)^{\frac{3}{4}} \right) H(v_0 t - r) \right] \quad (2)$$

Here the term within Dirac delta function represents direct wave and other term indicates

scattered waves. v_0 describes the mean S-wave velocity while g_0 is the scattering coefficient.

Possible discrepancy between predicted (Eq. 1) and observed energy densities for each event at each station with N_{ij} time samples (index k) in a specific frequency band can be minimized using:

$$\epsilon(g) = \sum_{i,j,k}^{N_S, N_S, N_{ij}} (\ln E_{ijk}^{obs} - \ln E_{ijk}^{mod}(g))^2 \quad (3)$$

Here, the number of stations (index i) and events (index j) are shown by N_S and N_E , respectively. Optimization of g will be achieved when

$$\ln E_{ijk}^{obs} = \ln E_{ijk}^{mod} \quad (4) \quad \text{or}$$

$$\ln E_{ijk}^{obs} = \ln G t_{ijk}, r_{ijk}, g + \ln R_i + \ln W_j - b t_{ijk} \quad (5)$$

Equation 5 simply define an overdetermined inversion problem with $\sum_{i,j} N_{ij}$ number equation systems and with $N_S + N_E + 1$ variables and thus b , R_i , and W_j can be solved via a least-squares technique. $\epsilon(g)$ can be defined as sum over the squared residuals of the solution.

Eulenfeld and Wegler (2016) present a simple recipe to perform inversion:

(i) Calculate Green's functions through the analytic approximation of the solution for 3-D isotropic radiative transfer (e.g. Paasschens 1997; Sens-Schönfelder and Wegler, 2006) by using fixed scattering parameters and minimize equation 5 to solve for b , R_i , and W_j via a weighted least-squares approach.

(ii) Calculate $\epsilon(g)$ using equation 3.

(iii) Repeat (i) and (ii) by selecting different g to find the optimal parameters g , b , R_i and W_j that finally minimize the error function ϵ .

In Fig. 3 an example for the minimization process that was applied at five different frequency bands is displayed for one selected event at recorded stations of the CD-CAT project.

Minimization described above for different frequencies will yield unknown spectral source energy term, W_j as well as site response, R_i and attenuation parameters, b , and g that will satisfy optimal fitting between observed and predicted coda wave envelopes. Example for this fitting can be seen in Figure 4. The present study deals with frequency dependency of W_j since this information can be later useful to obtain source displacement spectrum and thus seismic moment and moment magnitudes of analyzed earthquakes using the formula of the S -wave source displacement spectrum for a double-couple source in the far-field, which is given by Sato et al. (2012):

$$\omega M(f) = \sqrt{\frac{5\rho_0 v_0^5 W}{2\pi f^2}} \quad (6)$$

The relation between the obtained source displacement spectrum and seismic moment value was earlier described in Abercrombie (1995) by:

$$\omega M(f) = M_0 \left(1 + \left(\frac{f}{f_c} \right)^n \right)^{-\frac{1}{\gamma}} \quad (7)$$

where n is related to the high-frequency fall-off and γ is known as shape parameter that controls the sharpness of spectrum at corner frequency between the constant level M_0 (low frequency part) and the fall-off with f^{-n} (high frequency part). Taking logarithm of equation 7 gives:

216

217
$$\ln \omega M(f) = \ln M_0 - \frac{1}{\gamma} \ln \left(1 + \left(\frac{f}{f_c} \right)^{\gamma c} \right) \quad (8)$$

218

219 Eq. 8 describes an optimization problem of which data forms observed source displacement
220 spectrum and four source parameters, M_0 , γ , n , and f_c are the unknown model parameters that
221 can be resolved in a simultaneous least-squares inversion of the equation 8. Finally moment
222 magnitude, M_w can be calculated from modeled source parameters, seismic moment, M_0
223 using a formula given by Hanks and Kanamori (1979):

224

225
$$M_w = \frac{2}{3} \log_{10} M_0 - 6.07 \quad (9)$$

226

227 *4. Results and Discussions*

228 *4.1 Coda wave source spectra*

229 Figure 5 displays observed values of source spectra established by inserting inverted spectral
230 source energy term W at each frequency in Eq. 6 for all analyzed events. Each curve in this
231 figure represents model spectrum estimate based on inversion procedure described in previous
232 section. Modeled spectrum characteristics computed for 487 local earthquakes of which
233 lateral distribution is presented in Figure 2 suggest, in general, that we were able to obtain
234 typically expected source displacement spectrum with a flat region around the low frequency
235 limit and decaying behaviour above a corner frequency.

236

237 Owing to the multiple-scattering process within small scale heterogeneities that makes coda
238 waves gain an averaging nature, the variation in coda amplitudes due to differences source
239 radiation pattern and path effect are reduced (Walter et al., 1995; Mayeda et al., 2003).
240 Eulenfeld and Wegler (2016) found that radiation pattern would have only a minor influence

on the S-wave coda while it might disturb attenuation models inferred from the direct S-wave analyses unless the station distribution relative to the earthquakes indicates a good azimuthal coverage. A peak-like source function assumption for small earthquakes that are utilized in the present work was earlier proven to be adequate in early application of the coda-wave fitting studies (e.g. Sens-Schönfelder and Wegler, 2006; Gaebler et al., 2015; and Eulenfeld and Wegler, 2016).

Conventional approaches (e.g. Abercrombie, 1995; Kwiitek et al., 2011) to estimate source parameters such as corner frequency, seismic moment, high-frequency fall-off through fitting of observed displacement spectra observed at a given station in an inversion scheme could be misleading since these methods usually: (i) assume a constant value of attenuation effect (no frequency variation) defined by a factor $\exp(-\pi f t Q^{-1})$ over the spectrum, (ii) and assume omega-square model with a constant high-frequency fall-off parameter, $n=2$. Following Sens-Schönfelder and Wegler (2006) and Eulenfeld and Wegler (2016), however, we estimate attenuation parameters (intrinsic and scattering) separately within a simultaneous inversion procedure in which high-frequency fall-off parameter varies. This is fairly consistent with early studies (e.g. Ambeh and Fairhead, 1991; Eulenfeld and Wegler, 2016) where significant deviations from the omega square model ($n>3$) were reported implying that the omega-square model as a source model for small earthquakes must be reconsidered in its general acceptance. Earlier it has been well-observed that the source spectra, especially, for large earthquakes could be better explained by models of two corner frequencies (e.g., Papageorgiou and Aki, 1983; Joyner, 1984; Atkinson, 1990). Recently, Denolle et al. (2016) observed that conventional spectral model of a single-corner frequency and high-frequency fall-off rate could not explain P wave source spectra of thrust earthquakes with magnitude Mw 5.5 and above. Instead, they suggested the double-corner-frequency model for large

global thrust earthquakes with a lower corner frequency related to source duration and with an upper corner frequency suggesting a shorter time scale unrelated to source duration, which exhibits its own scaling relation. Uchide and Imanishi (2016) reported similar differences from the omega-square model would be valid also for smaller earthquakes by using spectral ratio technique that involves empirical Green's function (EGF) events to avoid having a complete knowledge of path and site effects for shallow target earthquakes (M_W 3.2–4.0) in Japan. The source spectra for many of the target events in their study suggested a remarkable discrepancy from the omega-square model for relatively small earthquakes. They explained such differences by incoherent rupture due to heterogeneities in fault properties and applied stress, the double-corner-frequency model, and possibility of a high-frequency falloff exponent value slightly higher than 2. In our case, the smallest event was with M_W -coda larger than 2.0, thus we had no chance to make a similar comparison, however, high-frequency fall-off parameters varied from $n=0.5$ to $n=4$. A notable observation in the distribution of n was $n=2$ or $n=2.5$ would be better explained for earthquakes with M_W -coda >4.0 whereas the smaller magnitudes exhibited more scattered pattern of variation in n (Figure 7). Eulenfeld and Wegler (2016) claimed that the use of separate estimates of the attenuation or correction for path effect via empirically determined Green's function would be better strategy in order to invert station displacement spectra for source parameters. This is mainly because smaller earthquakes (with $n>2$), in particular, assuming omega-square model can distort the estimates of corner frequency and even seismic moment especially in regions where Q is strongly frequency dependent.

4.2 Coda wave –derived magnitude vs. M_L catalogue magnitude

A scatter plot between catalogue magnitudes based on local magnitudes (M_L) and our coda-derived magnitudes (M_W -coda) that are inferred from resultant frequency dependent source

displacement spectra and thus seismic moment (e.g. Eq. 9) is shown in Fig. 6. Such comparison suggests an overall coherency between both types of magnitudes. This implies very simple model of a first-order approximation for S-wave scattering with isotropic acoustic radiative transfer approach can be efficient to link the amplitude and decaying character of coda wave envelopes to the seismic moment of the source.

In the present study, a linear regression analyses performed between M_W -coda and M_L magnitudes (Fig. 5) resulted in an empirical formula that can be employed to convert local magnitudes into coda-derived moment magnitude calculation of local earthquakes in this region:

$$M_{W-coda} = 1.1655 \pm 0.0337 \times M_L - 0.7085 \pm 0.0128 \quad (10)$$

Bakun and Lindh (1977) empirically described the linear log seismic moment-local magnitude relation between seismic moments (M_0) and local magnitudes (M_L) for earthquakes near Oroville, California. Beside this several other studies investigated to find an optimum relation between M_W and M_L by implementing linear and/or non-linear curve-fitting approaches. Malagnini and Munafò proposed two different linear fits separated by a crossover $M_L=4.31$ could represent M_L - M_W data points obtained from earthquakes of the central and northern Apennines, Italy. Several coefficient of regression analyses in their fits account for the combined effects of source scaling and crustal attenuation as well as regional attenuation, focal depth, and rigidity at source. Goertz-Allmann et al. (2011), for instance, introduced hybrid type of scaling relation that is linear below M_L 2 and above M_L 4 and a quadratic relation in between ($2 \leq M_L \leq 4$) for earthquakes in Switzerland detected between 1998 and 2009. Edwards and Rietbrock (2009) employed a second-order polynomial equation to relate

local magnitudes routinely reported in the Japan Meteorological Agency (JMA) magnitude and moment magnitude. More recently, using multiple spectral ratio analyses Uchide and Imanishi (2018) estimated relative moment magnitudes for the Fukushima Hamadori and the northern Ibaraki prefecture areas of Japan and reported a quadratic form of correlation between JMA magnitudes and moment magnitudes. Resultant empirical curve in Uchide and Imanishi (2018) implied a considerable discrepancy between the moment magnitudes and the JMA magnitudes, with a slope of 1/2 for microearthquakes suggesting possible biases introduced by anelastic attenuation and the recording by a finite sampling interval.

Apparent move-out in Fig. 5 and Eq. 10, presumably stems from the use of different magnitude scales for comparison. Conventional magnitudes scales such as M_L , m_b inferred from phase amplitude measurements are seemingly sensitive to attenuation and 2D variation along the path (Pasyanos et al., 2016). Unlike local magnitude scales, seismic moment-based moment magnitude (M_w) essentially represents a direct measure of the strength of an earthquake caused by fault slip and is estimated from relatively flat portion of source spectra at lower frequencies that can be less sensitive to the near surface attenuation effects. The consistency between coda-derived moment magnitude and local magnitude scales for the earthquakes with M_w -coda > 3.0 indicates that our non-empirical approach successfully worked in this tectonically complex region. This observation is anticipated, for relatively large earthquakes, since more energy will be characteristic at lower frequencies. We observed similar type of consistency in early studies that investigate source properties of local and regional earthquakes based on empirical coda methods with simple 1-D radially symmetric path correction (e.g. Eken et al., 2004; Gök et al., 2016). Coda waves-derived source parameters were obtained with high-precision in Mayeda et al. (2005), Phillips et al. (2014), Pasyanos et al. (2016) following the use of 2-D path-corrected station techniques to

consider the amplitude-distance relationships. Observable outliers in Figure 5, for the events with less than M_w 3.5, however, can be attributed to the either possible biases on local magnitude values taken from the catalogue or small biases on our intrinsic (Q_i^{-1}) and scattering (Q_s^{-1}) attenuation terms. One another possible contribution to such mismatch might be associated to the influences of mode conversions between body and surface waves or surface-to-surface wave scattering (e.g. Wu & Aki 1985) that are not restricted to low frequencies ($<1\text{Hz}$) (Sens-Schönfelder and Wegler, 2006).

5. Conclusions

This study provides an independent solution for estimating seismic source parameters such as seismic moment and moment magnitude for local earthquakes in central Anatolia without requiring *a priori* information on reference events with waveform modelling results to be used for calibration or *a priori* information on attenuation for path effect corrections. In this regard, the approach used here can be easy and useful tool for investigation of source properties of local events detected at temporal seismic networks. Moreover, seismic moment can be approximated via waveform modelling methods but due to the small-scale heterogeneities of the media that waves propagate, it is often a hard task to establish Green's function for small earthquakes ($M_L < 3.5$). An analytical expression of energy density Green's function in a statistical manner employed in the present work enables neglecting the interaction of the small-scale inhomogeneities with seismic waves as this can be practical for seismic moment calculations of small events that may pose source energy at high-frequency. It is noteworthy to mention that our isotropic scattering assumption does not consider anisotropic case, which could be valid for real media, but still provides a simple and effective tool to define the transport for the anisotropic case since the estimated scattering coefficient can be interpreted as transport scattering coefficient. An averaging over S-wave window

enables to overcome biases caused by using unrealistic Green's function (Gaebler *et al.* 2015). Since the present study mainly focuses on source properties of local earthquakes in the study area, scattering and intrinsic attenuation properties that are other products of our coda envelope fitting procedure will be examined in details within a future work. Finally, the empirical relation developed between M_W -coda and M_L will be a useful tool for quickly converting catalogue magnitudes to moment magnitudes for local earthquakes in the study area.

Data and resources

The python code used for carrying out the inverse modeling is available under the permissive MIT license and is distributed at <https://github.com/trichter/qopen>. We are grateful to the IRIS Data Management Center for maintaining, archiving and making the continuous broadband data used in this study open to the international scientific community.

Acknowledgement

The facilities of IRIS Data Services, and specifically the IRIS Data Management Center, were used for access to waveforms, related metadata, and/or derived products used in this study. IRIS Data Services are funded through the Seismological Facilities for the Advancement of Geoscience and EarthScope (SAGE) Proposal of the National Science Foundation under Cooperative Agreement EAR-1261681. Data for the CD-CAT experiment (https://doi.org/10.7914/SN/YB_2013) are available from the IRIS Data Management Center at <http://www.iris.edu/hq/>. Tuna Eken acknowledge financial support from Alexander von Humboldt Foundation (AvH) towards computational and peripherals resources. I am grateful to the Topical Editor Charlotte Krawczyk for handling the revision process and Takahiko Uchide for his valuable opinions on the improvement of manuscript.

391 *References*

- 392 Abercrombie, R.E.: Earthquake source scaling relationships from -1 to 5 ML using
393 seismograms recorded at 2.5-km depth, *J. geophys. Res.*, 100(B12), 24 015–24 036,
394 1995.
- 395 Aki, K., and Chouet., B.: Origin of coda waves: Source, attenuation, and scattering effects, *J.*
396 *Geophys. Res.* 80, 3322–3342, 1975.
- 397 Atkinson, G. M.: A comparison of eastern North American ground motion observations with
398 theoretical predictions, *Seismol. Res. Lett.* 61, 171–180, 1990.
- 399 Bakun, W.H. and Lindh, A.G.: Local Magnitudes, Seismic Moments, and Coda Durations for
400 Earthquakes Near Oroville, California, *Bulletin of the*
401 *Seismological Society of America*. Vol.67, No.3, pp. 615-629, 1977.
- 402 Bozkurt, E.: Neotectonics of Turkey—A synthesis: *Geodinamica Acta*, v. 14, p. 3–30, 2001.
- 403 Bulut, F., Bohnhoff, M., Eken, T., Janssen, C., Kılıç, T., and Dresen, G.: The East Anatolian
404 fault zone: Seismotectonic setting and spatiotemporal characteristics of seismicity based
405 on precise earthquake locations: *Journal of Geophysical Research*, v. 117, B07304,
406 <https://doi.org/10.1029/2011JB008966>, 2012.
- 407 Çemen, I., Göncüoğlu, M.C., and Dirik, K.: Structural evolution of the Tuz Gölü basin in central
408 Anatolia, Turkey: *Journal of Geology*, v. 107, p. 693–706, [https://doi.org/10.1086](https://doi.org/10.1086/314379)
409 [/314379](https://doi.org/10.1086/314379), 1999.
- 410 Çubuk Y, Yolsal-Çevikbilen S, Taymaz, T.: Source parameters of the 20052008 Bal'aSirapinar
411 (central Turkey) earthquakes: Implications for the internal deformation of the Anatolian
412 plate. *Tectonophysics* 635(Supplement C) :125 – 153, 2014.
- 413 Denolle, M. A., and Shearer, P.M.: New perspectives on self-similarity for shallow thrust
414 earthquakes, *J. Geophys. Res. Solid Earth*, 121, 6533–6565, 2016.

415 Edwards, B., & Rietbrock, A.: A comparative study on attenuation and source-scaling relations
 416 in the Kantō, Tokai, and Chubu regions of Japan, using data from Hi-net and KiK-net.
 417 Bulletin of the Seismological Society of America, 99, 2435–2460, 2009.

418 Eken, T., Mayeda, K., Hofstetter, A., Gök, R., Orgülü, G. and Turkelli, N.: An application of the
 419 coda methodology for moment-rate spectra using broadband stations in Turkey.
 420 Geophys. Res. Lett, 31, L11609, 2004.

421 Eulenfeld, T. and Wegler, U.: Measurement of intrinsic and scattering attenuation of shear
 422 waves in two sedimentary basins and comparison to crystalline sites in Germany,
 423 Geophys J Int., 205(2):744-757, 2016.

424 Eulenfeld, T. and Wegler, U.: Crustal intrinsic and scattering attenuation of high-frequency
 425 shear waves in the contiguous United States. J Geophys., Res, 122, 2017.

426 Favreau, P., and Archuleta, R.J.: Direct seismic energy modelling and application to the 1979
 427 Imperial Valley earthquake, Geophys. Res. Lett., 30, 1198, 2003.

428 Gaebler, P.J., Eulenfeld, T. & Wegler, U.: Seismic scattering and absorption parameters in the
 429 W-Bohemia/Vogtland region from elastic and acoustic radiative transfer theory,
 430 Geophys. J. Int., 203(3), 1471–1481, 2015.

431 Gaebler, P.J., Eken, T., Bektaş, H.Ö, Eulenfeld, T., Wegler, U., Taymaz, T.: Imaging of Shear
 432 Wave Attenuation Along the Central Part of the North Anatolian Fault Zone, Turkey,
 433 submitted to the Journal of Seismology, 2018.

434 Goertz-Allmann, B. P., Edwards, B., Bethmann, F., Deichmann, N., Clinton, J., Fäh, D., &
 435 Giardini, D.: A new empirical magnitude scaling relation for Switzerland. Bulletin of the
 436 Seismological Society of America, 101, 3088–3095, 2011.

437 Gök, R., Kaviani, A., Matzel, E. M., Pasyanos, M. E., Mayeda, K., Yetirmishli, G., El-Hussain,
 438 I., Al-Amri, A., Al-Jeri, F., Godoladze, T., Kalafat, D., Sandvol, E. A., and Walter,

439 W.R.: Moment Magnitudes of Local/Regional Events from 1D Coda Calibrations in the
 440 Broader Middle East Region. *Bull Seismol Soc Am.*, 106(5):1926-1938, 2016.
 441 Gusev, A.A. & Abubakirov, I.R.: Simulated envelopes of non-isotropically scattered body
 442 waves as compared to observed ones: another manifestation of fractal heterogeneity,
 443 *Geophys. J. Int.*, 127(1), 49–60, 1996.
 444 Hanks, T.C. and Kanamori, H.: A moment magnitude scale, *J. Geophys., Res.*, 84, 2348–2350,
 445 1979.
 446 Izgi, G., Eken, T., Gaebler, P., and Taymaz, T.: Frequency-Dependent Shear Wave Attenuation
 447 Along the Western Part of the North Anatolian Fault Zone, *Geophysical Research*
 448 *Abstracts*, Vol. 20, EGU2018-629-2, 2018.
 449 Kaymakci, N. Inceöz, M. Ertepinar, P.: 3D architecture and Neogene evolution of the Malatya
 450 Basin: inferences for the kinematics of the Malatya and Ovacik Fault Zones. *Turkish*
 451 *Journal of Earth Sciences*, 15, 123-154, 2006.
 452 Kwiatek, G., Plenkers, K. & Dresen, G.: 2011. Source parameters of pico-seismicity recorded at
 453 Mponeng Deep Gold Mine, South Africa: implications for scaling relations, *Bull. seism.*
 454 *Soc. Am.*, 101(6), 2592–2608, 2011.
 455 Malagnini, L., Mayeda, K., Akinci, A., and Bragato, P. L.: Estimating absolute site effects,
 456 *Bull. Seismol. Soc. Am.* 94, no. 4, 1343–1352, 2004.
 457 Malagnini, L., and Munafò, I.: On the Relationship between M_L and M_w in a Broad Range: An
 458 Example from the Apennines, Italy, *Bulletin of the Seismological Society of America*,
 459 Vol. 108, No. 2, pp. 1018–1024, 2018.
 460 Mayeda, K., and Walter, W.R.: Moment, energy, stress drop, and source spectra of western
 461 United States earthquakes from regional coda envelopes, *J. Geophys. Res.* 101, 11,195–
 462 11,208, 1996.

463 Mayeda, K., Hofstetter, A., O'Boyle, J.L., and Walter, W.R.: Stable and transportable regional
 464 magnitudes based on coda-derived moment-rate spectra, *Bull. Seismol. Soc. Am.* 93,
 465 224–239: 2003.

466 Mayeda, K., Malagnini, L., Phillips, W. S., Walter, W. R., and Dreger, D.: 2D or not 2D, that is
 467 the question: A Northern California Test. *Geophysical Research Letters*, 32(12), 2005.

468 Morasca, P., Mayeda, K., Malagnini, L. and Walter, W.R.: Coda and direct-wave attenuation
 469 tomography in northern Italy, *Bull Seismol Soc Am.*, v. 98, pages, 1936-1946, 2004.

470 Morasca, P., Mayeda, K., Gök, R., Phillips, W.S., and Malagnini, L.: Coda-derived source
 471 spectra, moment magnitudes and energy-moment scaling in the western Alps, *Geophys.*
 472 *J. Int.*, 160, 263–275, 2008.

473 Paasschens, J.: Solution of the time-dependent Boltzmann equation, *Phys. Rev. E*, 56(1), 1135–
 474 1141, 1997.

475 Papageorgiou, A., and Aki, K.: A specific barrier model for the quantitative description of
 476 inhomogeneous faulting and the prediction of strong ground motion I: Description of the
 477 model, *Bull. Seismol. Soc. Am.*, 73(3), 693–722, 1983.

478 Pasyanos, M. E., R. Gök, and Walter, W.R.: 2-D variations in coda amplitudes in the Middle
 479 East. *Bull. Seismol. Soc. Am.* 106, no. 5, 2016.

480 Phillips, W. S., Mayeda, K. M., and Malagnini, L.: How to invert multi-band, regional phase
 481 amplitudes for 2-d attenuation and source parameters: Tests using the usarray. *Pure and*
 482 *Applied Geophysics*, 171(3):469-484, 2014.

483 Portner, D.E., Delph, J.R., Biryol, C.B., Beck, S.L., Zandt, G., Özacar, A.A., Sandvol, E., and
 484 Türkelli, N.: Subduction termination through progressive slab deformation across
 485 Eastern Mediterranean subduction zones from updated P-wave tomography beneath
 486 Anatolia, *Geosphere*, 14(3): 907-925, 2018.

487 Przybilla, J. and Korn, M.: Monte Carlo simulation of radiative energy transfer in continuous
 488 elastic random mediathree-component envelopes and numerical validation. *Geophys J*
 489 *Int*, 173(2):566-576, 2008.

490 Rautian, T.G. & Khalturin, V.I.: The use of the coda for determination of the earthquake source
 491 spectrum, *Bull. Seism. Soc. Am.*, 68(4), 923–948, 1978.

492 Sato, H. and Fehler, M.C.: *Seismic Wave Propagation and Scattering in the Heterogeneous*
 493 *Earth*, Springer-Verlag, New York, 1998.

494 Sato, H., Fehler, M.C. & Maeda, T. *Seismic Wave Propagation, and Scattering in the*
 495 *Heterogeneous Earth*, 2nd edn, Springer: 2012.

496 Sens-Schönfelder, C. and Wegler, U.: Radiative transfer theory for estimation of the seismic
 497 moment. *Geophys J Int*, 167(3):1363-1372.

498 Taymaz, T., Jackson, J., Westaway, R.: Earthquake mechanisms in the Hellenic Trench near
 499 Crete. *Geophys. J. Int.* 102, 695–731, 1990.

500 Taymaz, T., Westaway, R., Reilinger, R.: Active faulting and crustal deformation in the eastern
 501 Mediterranean Region. *Spec. Issue Tectonophys.* 391 (1-4), 1–9. [http://](http://dx.doi.org/10.1016/j.tecto.2004.07.005)
 502 dx.doi.org/10.1016/j.tecto.2004.07.005, 2004.

503 Uchide, T., & Imanishi, K.: Small earthquakes deviate from the omega-square model as revealed
 504 by multiple spectral ratio analysis. *Bulletin of the Seismological Society of America*,
 505 106(3), 1357–1363, 2016.

506 Uchide, T., & Imanishi, K.: Underestimation of microearthquake size by the magnitude scale of
 507 the Japan Meteorological Agency: Influence on earthquake statistics. *Journal of*
 508 *Geophysical Research: Solid Earth*, 123, 606–620, 2018.

509 Yoo, S.-H., Rhie, J., Choi, H.-S., and Mayeda, K.: Coda-derived source parameters of
 510 earthquakes and their scaling relationships in the Korean Peninsula, *Bull. Seismol. Soc.*
 511 *Am.*, 101, 2388–2398, 2011.

512 Wu, R. and Aki, K.: The fractal nature of the inhomogeneities in the lithosphere evidenced from
513 seismic wave scattering, *Pure appl. Geophys.*, 123(6), 805–818, 1985.

514 Zeng, Y., Su, F. and Aki, K.: Scattering wave energy propagation in a random isotropic
515 scattering medium: 1. Theory, *J. Geophys. Res.*, 96(B1), 607–619, 1991.

516

517 *Figure Captions*

518 Figure 1. Major tectonic features of Turkey and its adjacent. The plate boundary data used
519 here is taken from Bird (2003). Subduction zones are black, continental transform faults are
520 red, continental rift boundaries are green, and spreading ridges boundaries are yellow. NAFZ,
521 EAFZ, and DSFZ are the North Anatolian Fault, East Anatolian Fault, and the Dead Sea fault,
522 respectively.

523

524 Figure 2. Epicentral distribution of all local events selected from the study area in the KOERI
525 catalogue. Gray circles represent earthquakes with poor quality that are not considered for the
526 current study while black indicates the location of local events with good quality. Red circles
527 among these events are 487 events used in coda wave inversion since they are successful at
528 passing quality criteria of further pre-processing procedure.

529

530 Figure 3. An example from the inversion procedure explained in chapter 3. Here coda
531 envelope fitting optimization is performed on band-pass filtered (8-16Hz) digital recordings
532 of an earthquake (2014 April 09, M_w -coda3.2) extracted for 7 seismic stations that operated
533 within the CD-CAT array. Large panel at the lower left-hand side displays the error function ϵ
534 as a function of g_0 . Thick blue cross here represent the optimal value of $g = g_0$. Other small
535 panels at upper and right-hand side show the least- squares solution of the weighted linear
536 equation system for the first 6 guesses and optimal guess for g_0 . There dots and gray curves

indicate the ratio between energy (E^{obs}) and the Green's function (G) obtained for direct S-waves and observed envelopes at various stations, respectively. Please notice that during this optimization process envelopes are corrected for the obtained site corrections R_i . The slope of linear curve at each small panel yields $-b$ and while its intercept W are the intrinsic attenuation and source related terms at the right-hand side of equation 5 part of the right-hand side of the equation system.

Figure 4. a) Results of the inversion of the 2014-April-09, M_w -coda3.2 earthquake: Sample fits between observed and calculated energy densities in the frequency band 0.5–1.0 Hz are given for 6 different stations (see upper right corner for event ID, station name, and distance to hypocenter). Note that light blue curves represent observed envelope. Smoothed observed calculated envelopes in each panel are presented by blue and red curves, respectively. Blue and red dots exhibit location of the average value for observed and calculated envelopes within the S-wave window, respectively. b) The same as in (a) obtained in the frequency band 4.0–8.0 Hz.

Figure 5. All individual observed (black squares) and predicted (gray curve) source displacement spectra observed at 72 stations from 487 local earthquakes in central Anatolia.

Figure 6: Scatter plot between local magnitudes (M_L) of analyzed events with coda waves-derived magnitudes (M_w -coda) of the same events. The outcome of a linear regression analysis yielded an empirical formula (e.g. Eq. 910) to identify the overall agreement represented by gray straight line. Yellow and red dashed lines indicate upper and lower limit of linearly fitting to that scatter.

Figure 7: Same scatter plot displayed in Fig. 6 color coded by estimated high-frequency fall-off parameter for each inverted event.

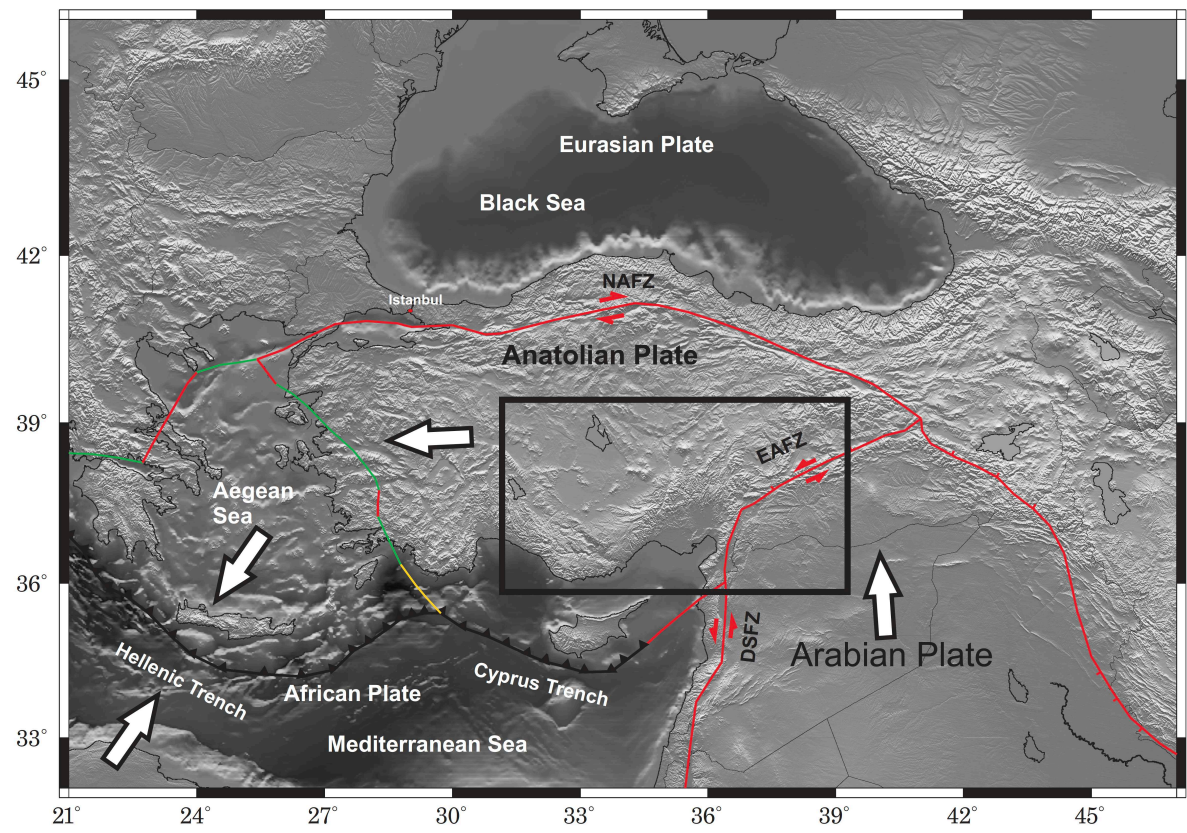


Figure 1.

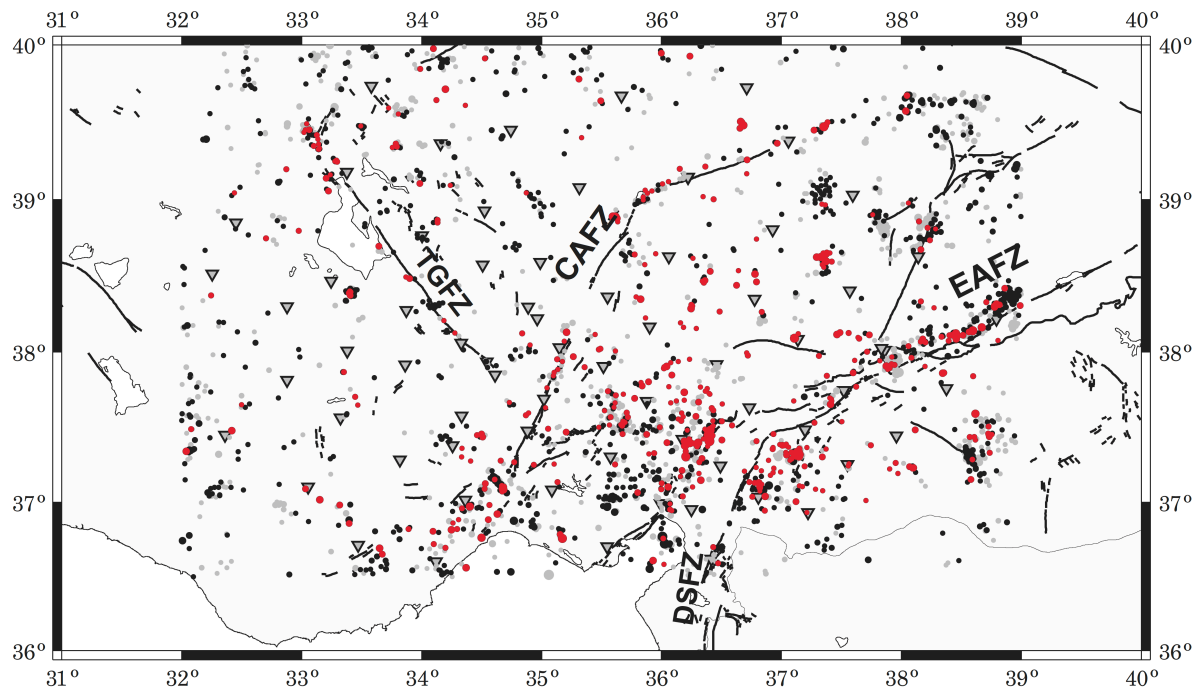


Figure 2.

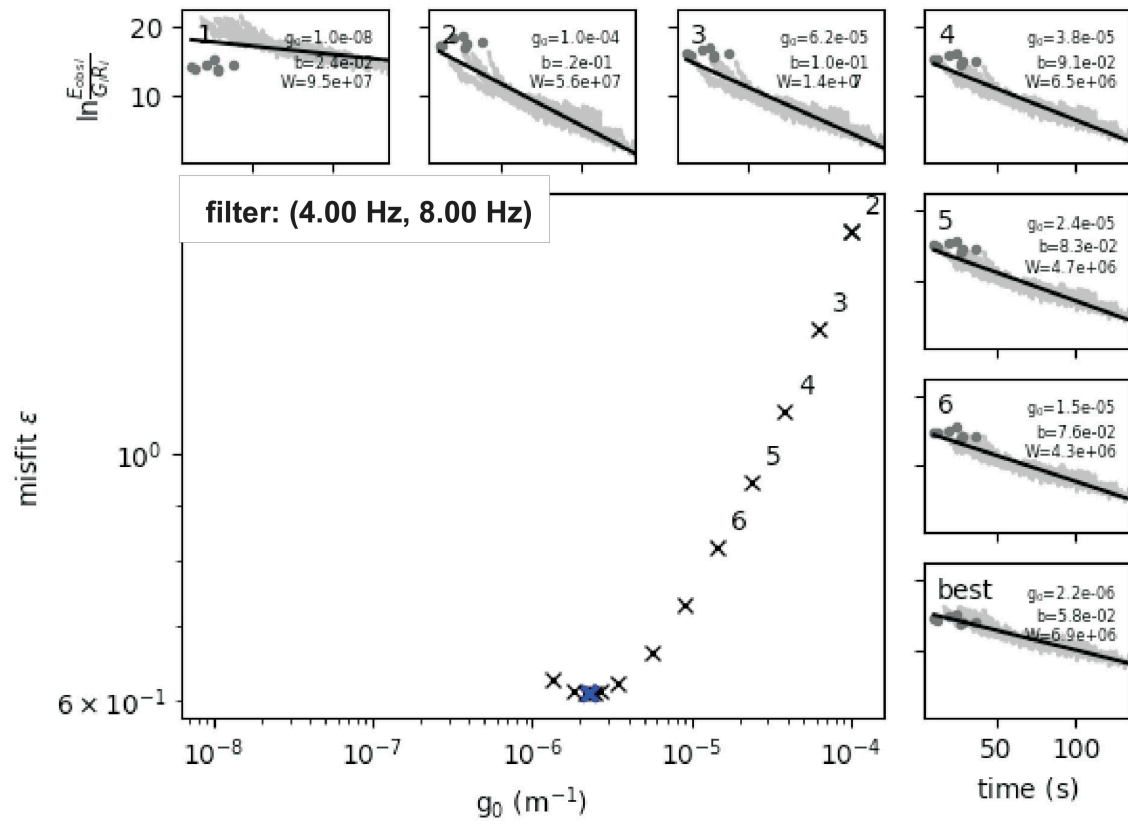


Figure 3.

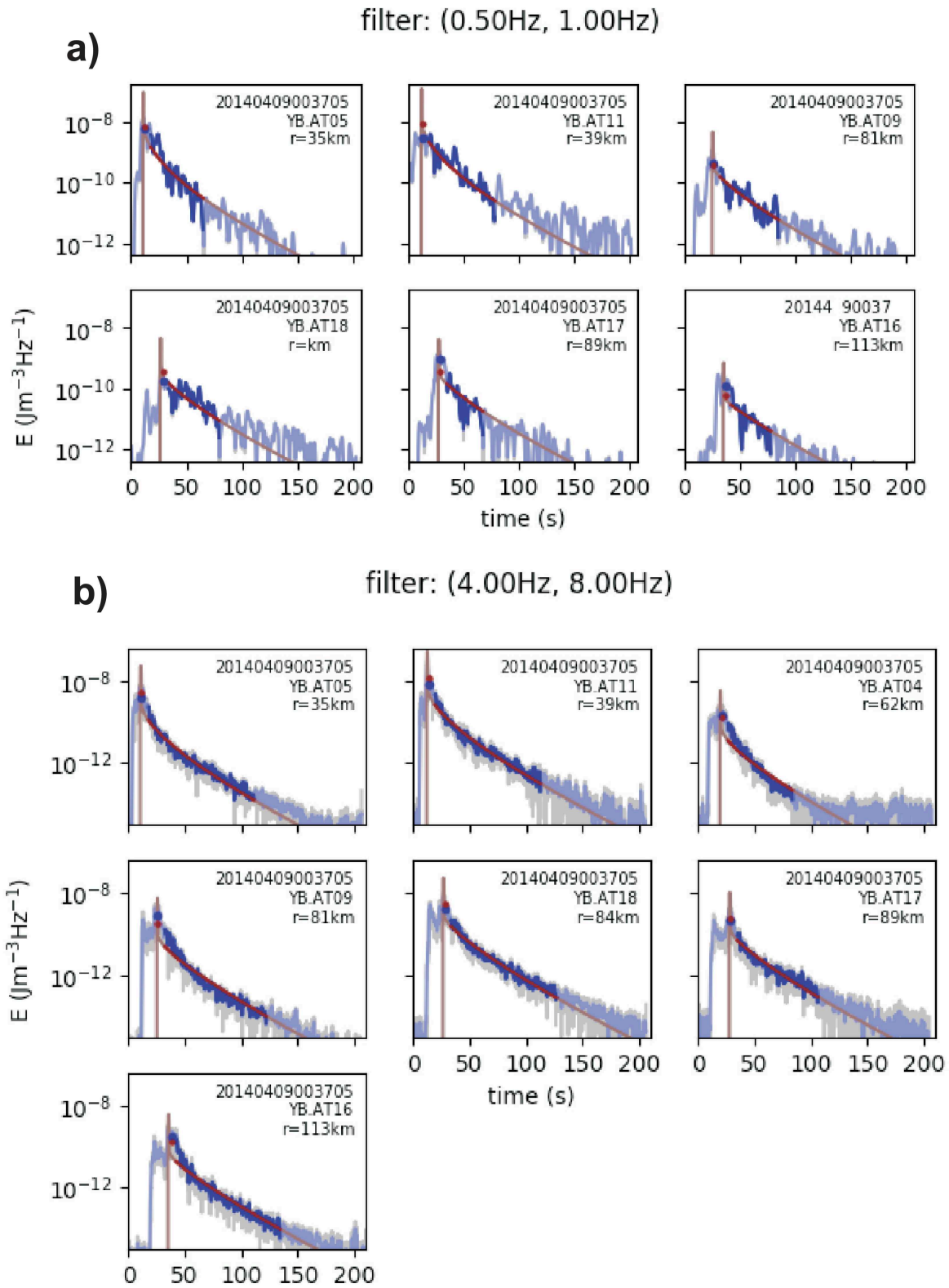
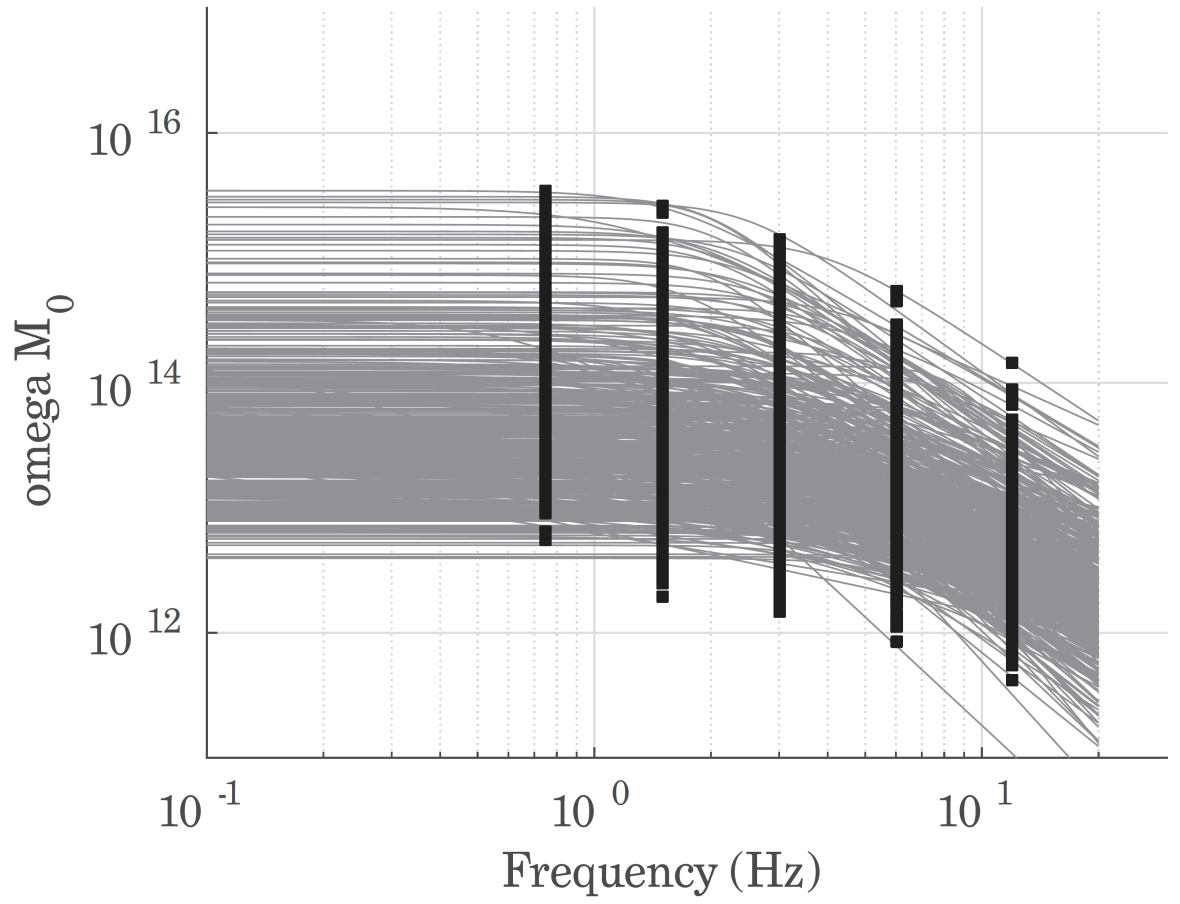


Figure 4.

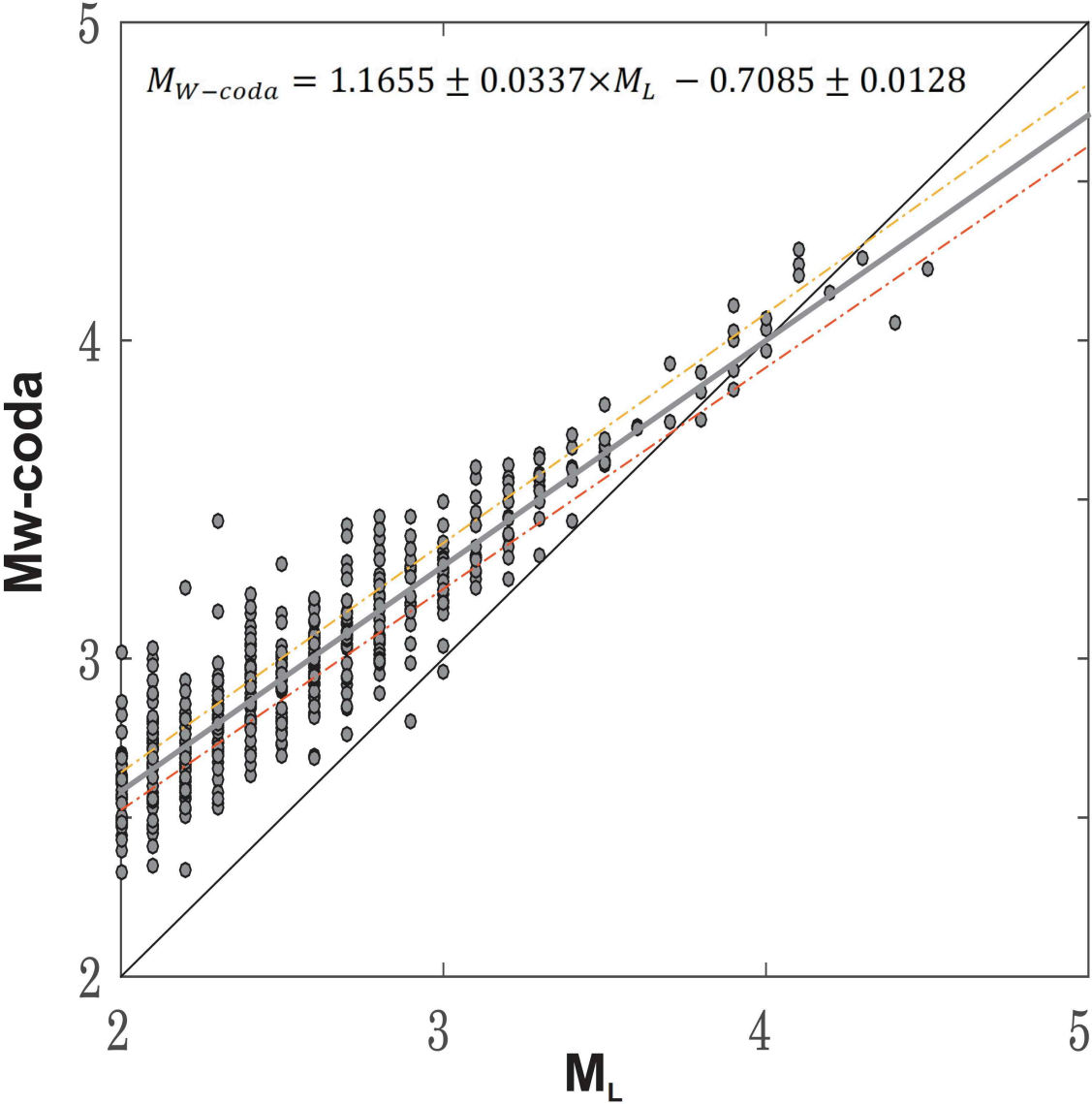
606
607
608
609
610



611
612
613
614
615
616
617
618
619
620
621
622
623
624
625
626
627
628
629
630
631

Figure 5.

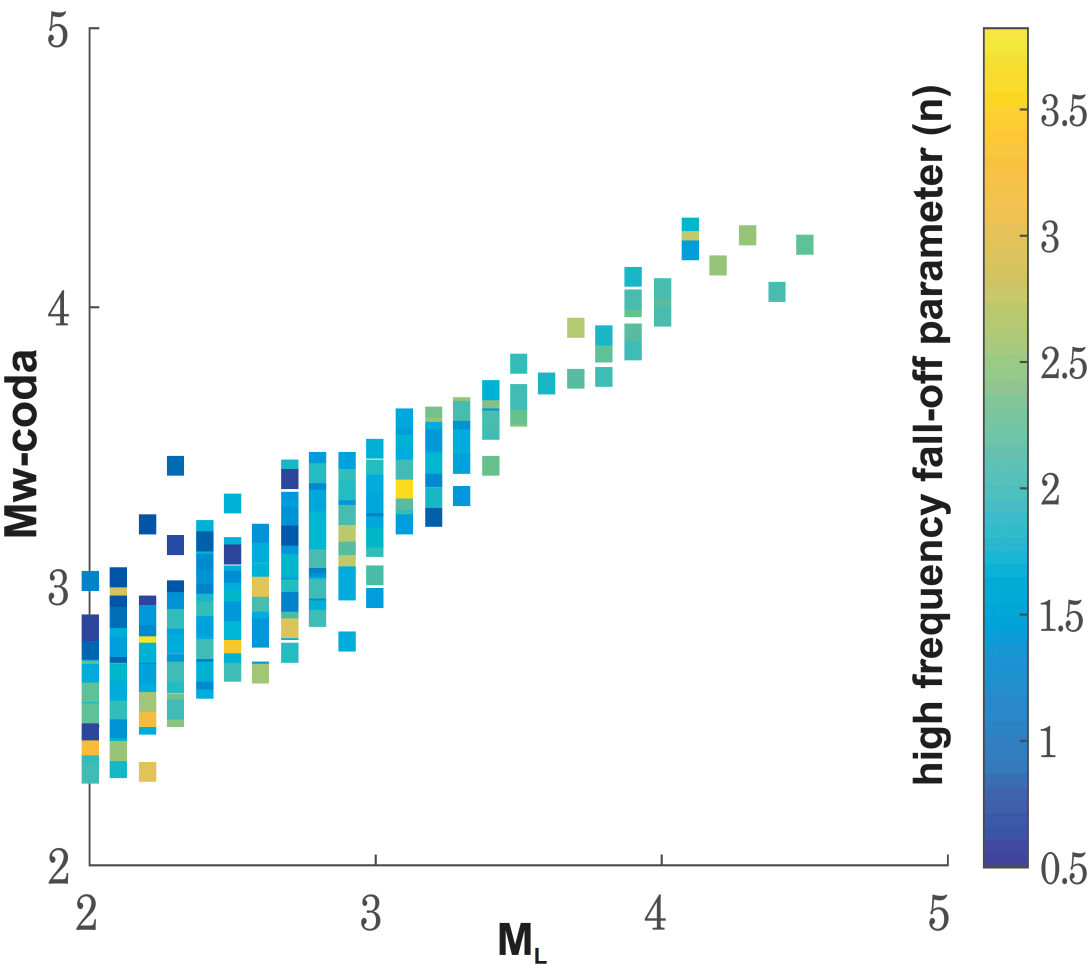
632
633
634
635
636
637



638
639
640
641
642
643
644
645
646
647
648
649
650
651

Figure 6.

652
653



654
655
656
657

Figure 7.